

AUV-Aided Localization of Underwater Acoustic Devices Based on Doppler Shift Measurements

Zijun Gong^{ID}, *Student Member, IEEE*, Cheng Li^{ID}, *Senior Member, IEEE*, Fan Jiang^{ID}, *Member, IEEE*,
and Jun Zheng^{ID}, *Senior Member, IEEE*

Abstract—The autonomous underwater vehicle (AUV)-aided localization techniques for underwater acoustic devices show promising applications in many scenarios, and most researches in this area are based on the time of arrival (ToA) or the time difference of arrival (TDoA) measurements. However, these measurements are not readily available. To develop a more universally applicable scheme, we investigate the possibility of employing the Doppler shift measurements for underwater localization of acoustic devices in this paper. To be specific, we employ a low-complexity algorithm for Doppler estimation, and prove that the estimation error can be well approximated by zero-mean Gaussian distribution. Based on the Doppler estimates, we can obtain a series of nonlinear equations. To solve them, we propose a two-phase linear algorithm to obtain high-accuracy position information of the target devices. Compared with the conventional iterative algorithms, the proposed one does not require initial estimate. Both the closed-form localization error and the Cramér-Rao lower bound are presented. They prove to be consistent for reasonably small Doppler estimation error. Besides, we conduct simulations to verify the theoretical analysis. Moreover, the complexity of the proposed algorithm only grows linearly with the number of Doppler shift measurements.

Index Terms—AUV, localization, Doppler shift, underwater, acoustic.

I. INTRODUCTION

WITH the growth of human ambition on ocean exploration, more and more underwater devices are deployed. These devices are used for environmental monitoring, resource exploitation, tsunami warning, wreck salvage, and so on. For many applications, a reliable underwater localization technique is very important. During the past several decades, many localization systems have been proposed,

including various system architectures and the localization algorithms. We will briefly review the existing work from these two aspects.

For the system architecture, the first choice is to deploy buoys on the sea surface of the target area [1]. These buoys are equipped with the GPS (Global Positioning System) receivers, and they can localize themselves at very low cost. Then, they serve as location-aware anchors, and broadcast their position and timing information through hydrophones. The underwater acoustic devices can receive the beacon signals for self-localization. This system is not economic for large underwater acoustic sensor networks, because the density of buoys should be comparable to that of the underwater sensors to ensure coverage. As a result, for large underwater acoustic sensor networks, the required number of buoys is quite significant. Another choice is to manually localize and synchronize some of the sensors, and use them as anchors for the localization of other sensors. Once a sensor is localized and synchronized, it can also serve as an anchor. This process iterates until the location information of all sensors is available. The major issue of this system is the low accuracy, as has been pointed out by [2]. To be specific, the positioning and timing accuracy of this system is highly dependent on the density of anchors. Due to the small number of initial anchors, the system performance is highly confined. Another problem of this architecture is that the positioning and timing error propagates in iterations [3]–[5]. Moreover, the clocks on sensors are generally low-cost ones with poor accuracy and subject to drifts, which means we need to calibrate them periodically for time of arrival (ToA)-based or time difference of arrival (TDoA)-based localization algorithms. Therefore, such systems are not efficient.

An alternative is to deploy autonomous underwater vehicles (AUVs) as mobile anchors [6]–[11]. The AUVs travel on the predefined trajectories, and broadcast beacon signals periodically. Any acoustic device in the communication range of the AUVs can receive the beacon signals and localize themselves through trilateration. This system can also work in the silent mode. To be specific, the target devices generate acoustic signals, while the AUVs stay silent. From the received signals, the AUVs can localize and track the target devices. Nowadays, some AUVs are solar-powered and suitable for long-endurance missions [12]. By employing AUVs, the number (or density, equivalently) of anchors can be boosted at negligible cost, leading to much improved accuracy [2]. Also, the AUVs can

Manuscript received June 10, 2019; revised September 26, 2019; accepted December 14, 2019. Date of publication January 8, 2020; date of current version April 9, 2020. This work was supported in part by the Natural Sciences and Engineering Research Council (NSERC) of Canada (Discovery Grant RGPIN- 2018-03792 and Postdoctoral Fellowship), and in part by the InnovateNL SensorTECH Grant 5404-2061-101. The associate editor coordinating the review of this article and approving it for publication was W. Ni. (Corresponding author: Cheng Li.)

Zijun Gong and Cheng Li are with the Faculty of Engineering and Applied Science, Memorial University of Newfoundland, St. John's, NL A1B 3X5, Canada (e-mail: zijun.gong@mun.ca; licheng@mun.ca).

Fan Jiang is with the Laboratory for Information and Decision Systems (LIDS), Massachusetts Institute of Technology (MIT), Cambridge, MA 02139 USA (e-mail: fjiang@mit.edu).

Jun Zheng is with the National Mobile Communications Research Laboratory, Southeast University, Nanjing 210096, China (e-mail: junzheng@seu.edu.cn).

Color versions of one or more of the figures in this article are available online at <http://ieeexplore.ieee.org>.

Digital Object Identifier 10.1109/TWC.2019.2963296

1536-1276 © 2020 IEEE. Personal use is permitted, but republication/redistribution requires IEEE permission.

See <https://www.ieee.org/publications/rights/index.html> for more information.

provide very good coverage by moving around in the area of interest. The positioning and timing error caused by the AUVs' movement is negligible, because their typical velocity is around 1.5 m/s [12], [13].

The localization algorithms are generally independent from the system architecture. These algorithms can be based on angle of arrival (AoA), ToA, TDoA, received signal strength (RSS), etc [14]. The ToA-based or TDoA-based ones are the most common, because the timing error is reported to be at the level of millisecond (ms) [15], leading to high positioning accuracy. The major challenges include stratification effects, long propagation delays, and energy constraints [16]. In many literatures, the underwater acoustic speed is assumed to be known, but as a matter of fact, it ranges from 1420 m/s to 1560 m/s [17]. In [11], the authors showed that a small uncertainty in acoustic speed will cause significant positioning error. Therefore, the acoustic speed should be treated as an extra unknown [18], [19]. In [11], the sequential time-synchronization and localization (STSL) algorithm was proposed, in which an AUV served as the mobile anchor. The AUV was assumed to be static during a short period of time due to its small velocity, which makes time synchronization easier. The maximum likelihood estimator was proposed in [20] for joint time synchronization and localization. However, due to the expensive computational complexity, a more efficient sub-optimal least square estimator was preferred. In addition, uncertainties of anchor's clock and location information were considered. The Cramér-Rao lower bounds (CRLBs) for both the accurate and inaccurate anchor information were derived.

In [21], it was argued that RSS-ranging based method should work better in aquatic environments than on ground. The reason is that RSS decreases faster with distance in underwater scenarios due to absorption, which leads to a strong correlation between the distance and the RSS. In [9], the authors installed directional antennas on an AUV, and two beams were generated on each side of the AUV. When a target device receives signals from the AUV for two consecutive beams, triangulation can be employed for localization. The largest advantage of this system is that sensors are passive, which will save energy and prolong battery life. In [22], the authors discussed the possibility of exploiting the Doppler effect for target course estimation, based on the assumption that the Doppler velocity log is available. In [23], the authors employed the Doppler shift measurements for node tracking.

Information fusion is also an interesting topic in this area. For example, the authors of [24] combined ToA and DoA for object localization through the Bayesian method. To be specific, the localization result is the coordinate that maximizes the likelihood function. In [25] and [26], the Doppler and ToA measurements were combined for localization.

In this paper, we propose a Doppler-based positioning system for the underwater acoustic devices. The AUV moves around in the area of interest and serves as a mobile anchor. This system can work in both proactive and passive modes. In the proactive mode, the AUV broadcasts its location information and a sinusoidal wave periodically. The target devices can localize themselves by receiving the signals from the

AUV. In the passive mode, the AUV stays silent and receives signals from the target devices. Based on the received signal, the AUV can estimate the location of the targets. Compared with the ToA-based or TDoA-based systems, the Doppler-based system has many advantages. First, localization accuracy can be boosted at very low cost. For example, assume that we need to increase the localization accuracy by one order. For the ToA-based or TDoA-based methods, the AUV needs to broadcast one hundred times faster (or longer). For the Doppler-based method, we just need to sample the sinusoidal wave $4.5 (\sqrt[3]{100} \approx 4.5)$ times longer, as will be shown in the performance evaluation part. Secondly, the TDoA and ToA based methods generally include time synchronization, which increases complexity. Thirdly, the ToA and TDoA measurements are not always available for various underwater localization applications, because our target does not necessarily have onboard communication modules. For example, assume that we want to track some moving objects, such as sharks and whales. We only need to attach a very simple tag that can generate sinusoidal acoustic waves for the Doppler-based localization system. However, for the ToA or TDoA based methods, we will need to install a much more complicated device for bidirectional communications. Another possible application is the searching of airplane wreckage in oceans. The flight recorder can be equipped with an acoustic tag that keeps generating sinusoid waves. As long as we know the rough location of the crash, many AUVs can be deployed in the area to search for the flight recorder.

In most related researches, Doppler shift is used to estimate the target's radial velocity, or combined with other metrics for target tracking. However, we will show that it is possible to conduct target localization exclusively dependent on Doppler estimates. Also, we will explore the performance bound of the system, and show that a simple iteration algorithm can achieve that bound. Different from the existing work, we incorporate the Doppler estimation process into the localization system, which brings two advantages. First, we can boost system performance by improving Doppler estimation accuracy. Second, we can obtain the statistics of the Doppler shift estimates, which allows us to develop more accurate localization algorithms, as we will show in latter discussions.

The work in this paper consists of two parts: the first part is the development and analysis of the Doppler estimation algorithm; the second part is the design, error analysis, and performance bound investigation of the Doppler-based localization system. In the first part, our major contributions lie in two aspects: 1) we proposed a refinement method to improve the accuracy of a low-complexity Doppler estimation algorithm; 2) the closed-form probability density function of the estimation error is derived. In the second part, there are also two major contributions: 1) we proposed a two-phase linear algorithm for Doppler-based underwater localization, and presented its closed-form localization error; 2) the CRLB of the proposed system is analyzed. Besides, we show that the proposed algorithm can asymptotically achieve the CRLB, both theoretically and numerically.

The rest of the paper is organized as follows. In Section II, we briefly introduce the Doppler shift estimation algorithm

and conduct comprehensive analysis of the estimation error. In Section III, the intuition and details of the proposed algorithm are presented. In Section IV, we thoroughly analyze the performance of the proposed system and algorithm, in terms of the CRLB, the localization error, and the computational complexity. In Section V, simulation results are presented and explained in details. The last section contains conclusions.

Notations: throughout the paper, the upper case bold letters represent matrixes while the lower case bold font denotes column vectors. $E\{\cdot\}$ is the expectation of any random number, vector or matrix, while $\text{var}\{\cdot\}$ denotes the variance of any random variable. The operator \circ indicates the element-wise multiplication of two matrixes or vectors of the same size. $\Re\{\cdot\}$ and $\Im\{\cdot\}$ give the real and imaginary parts of complex numbers, respectively. For an arbitrary vector \mathbf{a} , $\mathbf{a}[n]$ is the n -th element, while $\mathbf{a}[m : n]$ is a vector that contains the elements indexed from m to n . $\mathbf{A}[m, n]$ indicates the (m, n) -th element in \mathbf{A} . \mathbf{A}^T indicates the transpose of matrix \mathbf{A} . $|\cdot|$ is the norm of a vector, the absolute value of a number, or the determinant of a square matrix. $\text{cov}\{\mathbf{a}, \mathbf{b}\}$ gives the cross-covariance matrix of random vectors \mathbf{a} and \mathbf{b} . $\text{trace}\{\mathbf{A}\}$ denotes the trace of a diagonal matrix \mathbf{A} . For a square matrix \mathbf{A} , $\text{diag}\{\mathbf{A}\}$ gives a vector that contains its diagonal elements; for a vector \mathbf{a} , $\text{diag}\{\mathbf{a}\}$ returns a diagonal matrix with the elements of \mathbf{a} on its diagonal line. $\lfloor \cdot \rfloor$ rounds an arbitrary real number to the closest integer.

II. DOPPLER SHIFT ESTIMATION

For the proposed system, the estimation of Doppler shift is very important. In this section, we will introduce a widely adopted low-complexity Doppler estimation algorithm and propose a method to refine the results and improve estimation accuracy. The closed-form probability density function of the estimation error is derived. Before doing that, we briefly review the underwater acoustic channel model.

A. Underwater Acoustic Channel Model

The underwater acoustic channel model is generally given as [27]–[30]:

$$h(\tau, t) = \sum_{b=0}^{B-1} \rho_b(t) \delta(\tau - \tau_b(t)), \quad (1)$$

where B denotes the number of paths between the transmitter and the receiver, and these paths are indexed from 0 to $B-1$. Without loss of generality, we assume $b=0$ denotes the line-of-sight(LoS) path. $\rho_b(t)$ and $\tau_b(t)$ represent the gain and propagation delay of the b -th path at time t , and the propagation delay can be approximated by

$$\tau_b(t) = \tau_b - a_b t, \quad (2)$$

where a_b is often referred to as Doppler rate, and it describes how fast the delay of the b -th path varies. The arriving paths are ordered based on the time of arrival, i.e., $\tau_b(t) < \tau_{b+1}(t)$ for an arbitrary $b \in \{0, 1, \dots, B-2\}$.

We can assume that $\rho_b(t)$ is a constant for a relatively short period of time, because the coherence time for underwater

acoustic channels is on the level of seconds [28], [29]. The path loss model is given as [21], [31]

$$PL(d, f_c) = (d/d_0)^\gamma a(f_c)^{d-d_0}, \quad (3)$$

where d is the distance between the transmitter and the receiver, and d_0 is a reference distance. γ indicates the spreading loss, and it generally varies between 1 and 2. $a(f_c)$ is often referred to as the absorption coefficient, and it is a function of the carrier frequency f_c . In [31], we can see that the absorption coefficient increases with frequency piece-wise linearly. However, the bandwidth of underwater acoustic system is generally only several kHz (e.g., The AquaSeNT OFDM modem works in the bandwidth from 14 kHz to 20 kHz [32]), and $a(f_c)$ can be viewed as a constant.

B. Low-Complexity Doppler Shift Estimation

As we know, underwater acoustic signals generally experience the multi-path effect. As the AUV transmits a sinusoidal wave, the target device will receive a series of sinusoidal waves of different frequencies, i.e., different paths have different Doppler shifts. However, in all these paths, only the LoS one provides useful information concerning the location of the target. In this section, we will introduce the Doppler estimation method and analyze its performance by only considering the LoS path for the following reasons. First, the LoS path is much stronger than the others, and it is the major contributor of the Doppler shift [26], [29], [33]–[35]. Second, by increasing the sample number, the frequency resolution will be boosted and different paths can be well separated in frequency domain. As a matter of fact, the spectrum of every multi-path component can be approximated by a sinc function, which has one main lobe and many small side lobes. In the proposed method, only the main lobe of the LoS path is employed for Doppler estimation, which acts like a filter and can eliminate most multi-path components. As a result, only the side lobes of multi-path components will influence the estimation accuracy. Fortunately, the side lobes of the multi-path components lying on the two samples in the main lobe of the desired signals are very weak. We can prove that they are inversely proportional to the square of the sample number. As a result, they are negligible even when compared with noise. This issue has been discussed in details in [36], and the impact of the multi-path effect will be evaluated in simulations.

To begin with, assume that the onboard transmitter of the AUV broadcasts a sinusoidal wave at a frequency of f_c (in Hz). The target device samples the received signal at f_s (in Hz), and the sampled sequence \mathbf{s} will be

$$\mathbf{s}[n] = A \sin(2\pi(f_c + f_d)/f_s n + \theta) + \mathbf{n}_s[n], \quad (4)$$

where f_d is the Doppler shift, θ denotes unknown phase delay, and A is the amplitude of the received LoS signal. \mathbf{n}_s denotes noise vector, and the elements follow i.i.d. zero-mean Gaussian distribution, with a variance of σ^2 . Let $\omega = 2\pi(f_c + f_d)/f_s$, and we have

$$\mathbf{s}[n] = A \sin(\omega n + \theta) + \mathbf{n}_s[n]. \quad (5)$$

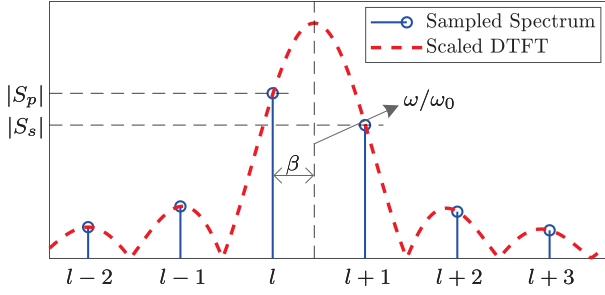


Fig. 1. When $0 \leq \beta < 0.5$, the peak appears on index l , while the sub-peak is on $l+1$.

For a sample number of N , we can obtain the discrete spectrum of \mathbf{s} as $\mathbf{s}_\omega = \text{DFT}\{\mathbf{s}\}$. The \tilde{n} -th element in \mathbf{s}_ω is

$$\mathbf{s}_\omega[\tilde{n}] = \frac{1}{N} \sum_{n=0}^{N-1} \mathbf{s}[n] e^{-j\tilde{n}n\omega_0}, \quad (6)$$

and $\omega_0 = 2\pi/N$. There must exist $l \in \{0, 1, \dots, N-1\}$ and $\beta \in [0, 1)$ that satisfy $\omega = (l + \beta)\omega_0$. (6) can then be rewritten as (7), shown at the bottom of the next page, in which θ_k and $\tilde{\theta}_k$ are given by

$$\begin{aligned} \theta_{\tilde{n}} &= \theta - \pi/2 + (N-1)(l + \beta - \tilde{n})\omega_0/2, \\ \tilde{\theta}_{\tilde{n}} &= -\theta - \pi/2 + (N-1)(-l - \beta - \tilde{n})\omega_0/2. \end{aligned} \quad (8)$$

The noise \mathbf{n}_ω is the DFT of \mathbf{n}_s , given by

$$\mathbf{n}_\omega[\tilde{n}] = \frac{1}{N} \sum_{n=0}^{N-1} \mathbf{n}_s[n] e^{-j\tilde{n}n\omega_0}. \quad (9)$$

\mathbf{s}_ω contains the samples from the discrete time Fourier transform (DTFT) of \mathbf{s} , and the sampling interval is $2\pi/N$. The DTFT of \mathbf{s} is very close to a scaled sinc function, and the main lobe has a width of $2\pi/N$. As a result, there are always two samples in the main lobe, as shown in Figure 1. The continuous curve is the scaled DTFT of \mathbf{s} (by a factor of $2\pi/N$), and the x-axis denotes the index on samples. The indexes of the two samples in the main lobe are l and $l+1$. When $0 \leq \beta < 0.5$, we have the peak value $S_p = \mathbf{s}_\omega[l]$, and its amplitude is

$$|S_p| = |\mathbf{s}_\omega[l]| \approx \frac{A \sin(\beta\pi)}{2\beta\pi}. \quad (10)$$

This approximation is achieved by two steps. The first step is to ignore the last two components in (7), because the strength of the second component is inversely proportional to N for $\tilde{n} = l$, while the noise component is at the level of $1/\sqrt{N}$, as will be discussed in Appendix VI. The second step is to employ $\sin(x) \approx x$ for $|x| \ll 1$. We will numerically show that this approximation is very accurate in later discussions.

Similar for the sub-peak $S_s = \mathbf{s}_\omega[l+1]$, the amplitude can be approximated by

$$|S_s| = |\mathbf{s}_\omega[l+1]| \approx \frac{A \sin(\beta\pi)}{2(1-\beta)\pi}. \quad (11)$$

Generally, S_p and S_s have the largest amplitudes in sequence $\mathbf{s}_\omega[\tilde{n}]$ ($0 \leq \tilde{n} \leq \lfloor N/2 \rfloor$). Based on (10) and (11), we can

estimate β as

$$\hat{\beta} = \frac{|S_s|}{|S_s| + |S_p|}. \quad (12)$$

It should be noted that both S_s and S_p follow Gaussian distribution, and they have the same variance. To analyze the distribution of estimation error, we rewrite (12) as

$$\hat{\beta} = \frac{|\bar{S}_s + \mathbf{n}_\omega[l+1]|}{|\bar{S}_p + \mathbf{n}_\omega[l]| + |\bar{S}_s + \mathbf{n}_\omega[l+1]|}, \quad (13)$$

where \bar{S}_p and \bar{S}_s are expectations of S_p and S_s , respectively. To simplify the notations, we define the noise components as follows:

$$\begin{aligned} n_1 &= \Re\{\mathbf{n}_\omega[l+1]\}, n_2 = \Im\{\mathbf{n}_\omega[l+1]\}, \\ n_3 &= \Re\{\mathbf{n}_\omega[l]\}, n_4 = \Im\{\mathbf{n}_\omega[l]\}. \end{aligned} \quad (14)$$

n_1, n_2, n_3, n_4 are irrelevant and identically distributed zero-mean Gaussian variables, with a variance of $\frac{\sigma^2}{2N}$, as has been discussed in Appendix VI. Also, R_s, I_s, R_p and I_p are given by

$$\begin{aligned} R_s &= \Re\{\bar{S}_s\}, I_s = \Im\{\bar{S}_s\}, \\ R_p &= \Re\{\bar{S}_p\}, I_p = \Im\{\bar{S}_p\}. \end{aligned} \quad (15)$$

Then, (13) can be further reorganized as

$$\hat{\beta} = \left(1 + \sqrt{\frac{(R_p + n_3)^2 + (I_p + n_4)^2}{(R_s + n_1)^2 + (I_s + n_2)^2}} \right)^{-1}. \quad (16)$$

Therefore, we can obtain the approximation of $\hat{\beta}$ through the Taylor expansion as

$$\begin{aligned} \hat{\beta} &\approx \frac{|\bar{S}_s|}{|\bar{S}_s| + |\bar{S}_p|} + \frac{R_s|\bar{S}_p|/|\bar{S}_s|}{(|\bar{S}_s| + |\bar{S}_p|)^2} n_1 + \frac{I_s|\bar{S}_p|/|\bar{S}_s|}{(|\bar{S}_s| + |\bar{S}_p|)^2} n_2 \\ &\quad - \frac{R_p|\bar{S}_s|/|\bar{S}_p|}{(|\bar{S}_s| + |\bar{S}_p|)^2} n_3 - \frac{I_p|\bar{S}_s|/|\bar{S}_p|}{(|\bar{S}_s| + |\bar{S}_p|)^2} n_4. \end{aligned} \quad (17)$$

In (17), we ignore the high-order components, because the absolute values of the noise components are inversely proportional to \sqrt{N} , which means they are negligible compared with \bar{S}_p and \bar{S}_s . In this case, $\hat{\beta}$ can be approximated by the Gaussian distribution, and the variance is

$$\text{var}\{\hat{\beta}\} \approx \frac{|\bar{S}_p|^2 + |\bar{S}_s|^2}{(|\bar{S}_s| + |\bar{S}_p|)^4} \cdot \frac{\sigma^2}{2N}. \quad (18)$$

For $\beta \in [0, 0.5)$, by employing the approximation in (10) and (11), (18) can be rewritten as

$$\text{var}\{\hat{\beta}\} \approx \frac{2\pi^2\sigma^2}{NA^2} \cdot (2\beta^2 - 2\beta + 1)\beta^2(1-\beta)^2/\sin^2(\beta\pi). \quad (19)$$

If we define $r_0(\beta) = \pi^2(2\beta^2 - 2\beta + 1)\beta^2(1-\beta)^2/\sin^2(\beta\pi)$, the variance of $\hat{\beta}$ will be

$$\text{var}\{\hat{\beta}\} \approx \frac{2\sigma^2 r_0(\beta)}{NA^2}. \quad (20)$$

On the other hand, for $\beta \in [0.5, 1)$, the peak and sub-peak values are given as

$$\begin{aligned} |S_p| &= |s_\omega[l+1]| \approx \frac{A \sin(\beta\pi)}{2(1-\beta)\pi} \text{ and} \\ |S_s| &= |s_\omega[l]| \approx \frac{A \sin(\beta\pi)}{2\beta\pi}. \end{aligned} \quad (21)$$

Then, β can be estimated as

$$\hat{\beta} = \frac{|S_p|}{|S_p| + |S_s|}, \quad (22)$$

and we can prove that the variance of $\hat{\beta}$ is identical to the results in (20).

It should be noted that β is estimated through (12) or (22), depending on whether β is smaller than 0.5 or not. However, we do not know the range of β before we estimate it. As a result, a practical question is how can we decide if we should use (12) or (22). To achieve this goal, we should first identify the peak value, and the sub-peak can be found on its left or right. These two values' indexes are l and $l+1$. Then, if $\beta \in (0, 0.5)$, we should have $|s_\omega[l]| > |s_\omega[l+1]|$; for $\beta \in (0.5, 1)$, $|s_\omega[l]| < |s_\omega[l+1]|$ should hold. Therefore, depending on the relative strength of $|s_\omega[l]|$ and $|s_\omega[l+1]|$, we can roughly decide if β is larger or smaller than 0.5.

C. Improve Doppler Shift Estimation Accuracy

When β is very close to 0 or 1, the algorithm described in the previous section is not reliable. To be specific, there is a high probability that the sub-peak cannot be correctly identified, because it is very weak. This scenario is illustrated in Figure 2. The sub-peak and the peak samples are indexed by l and $l_p = l+1$, respectively. In this case, β is very close to one, and the sub-peak is very weak and comparable to the other samples outside the main lobe. Without noise, two samples in the main lobe can be correctly identified. However, at the presence of noise, the sample strength at l_p+1 might be stronger than that at l , which leads to wrong estimation of l . To solve this problem, we propose the following method to improve estimation accuracy.

Let l_p be the index of the peak value in the spectrum, and there must exist $\beta_o \in [-0.5, 0.5)$ that satisfies $\omega = (l_p + \beta_o)\omega_0$. We have $l_p + \beta_o = l + \beta$, or $\beta_o = \beta - \lfloor \beta \rfloor$ equivalently, where $\lfloor \cdot \rfloor$ rounds an arbitrary real number to the closest integer. As shown in Figure 2, we take another two samples equally spaced around the peak sample, (i.e., S_1 and S_2). They can be computed through the following equation:

$$S_1 = \frac{1}{N} \sum_{n=0}^{N-1} s[n] e^{-j(l_p - 0.5)n\omega_0},$$

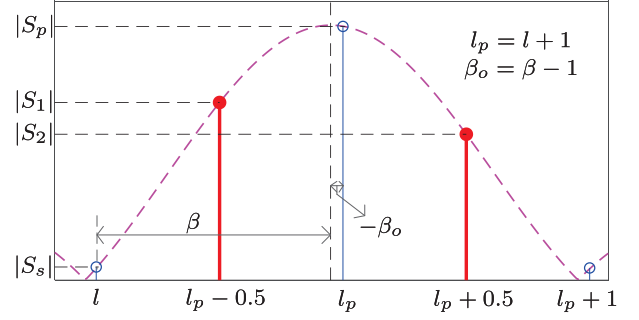


Fig. 2. The refinement of Doppler shift estimation.

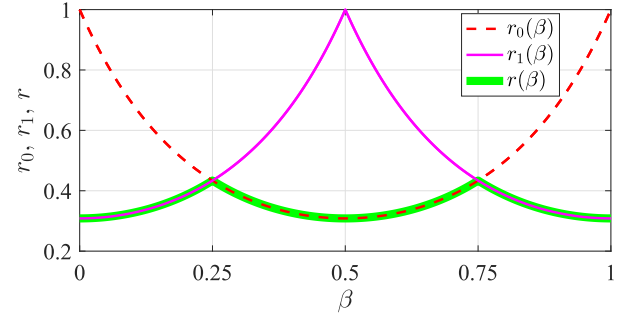


Fig. 3. The numerical result of $r_0(\beta)$, $r_1(\beta)$ and $r(\beta)$, with respect to β .

$$S_2 = \frac{1}{N} \sum_{n=0}^{N-1} s[n] e^{-j(l_p + 0.5)n\omega_0}, \quad (23)$$

and their absolute values can be approximated by

$$|S_1| \approx \frac{A \cos(\beta_o \pi)}{2(0.5 - \beta_o)\pi} \text{ and } |S_2| \approx \frac{A \cos(\beta_o \pi)}{2(0.5 + \beta_o)\pi}. \quad (24)$$

Based on (24), we can obtain the estimate of β_o as

$$\hat{\beta}_o = \frac{(|S_2| - |S_1|)/2}{|S_2| + |S_1|}. \quad (25)$$

By employing the first order Taylor expansion, we have the approximation as follows

$$\begin{aligned} \hat{\beta}_o \approx & \beta_o + \frac{R_2 |\bar{S}_1| / |\bar{S}_2|}{(|\bar{S}_1| + |\bar{S}_2|)^2} n_1 + \frac{I_2 |\bar{S}_1| / |\bar{S}_2|}{(|\bar{S}_1| + |\bar{S}_2|)^2} n_2 \\ & - \frac{R_1 |\bar{S}_2| / |\bar{S}_1|}{(|\bar{S}_1| + |\bar{S}_2|)^2} n_3 - \frac{I_1 |\bar{S}_2| / |\bar{S}_1|}{(|\bar{S}_1| + |\bar{S}_2|)^2} n_4. \end{aligned} \quad (26)$$

where \bar{S}_1 and \bar{S}_2 are the expectations of S_1 and S_2 , respectively, while R_1 , I_1 , R_2 and I_2 are defined as

$$\begin{aligned} R_1 &= \Re\{\bar{S}_1\}, I_1 = \Im\{\bar{S}_1\}, \\ R_2 &= \Re\{\bar{S}_2\}, I_2 = \Im\{\bar{S}_2\}. \end{aligned} \quad (27)$$

$$\begin{aligned} s_\omega[\tilde{n}] &= \frac{A}{N} \sum_{n=0}^{N-1} \frac{1}{2j} \left(e^{j(\omega n + \theta)} - e^{-j(\omega n + \theta)} \right) e^{-j\tilde{n}n\omega_0} + \mathbf{n}_\omega[\tilde{n}] \\ &= \frac{A}{2N} \left(e^{j\theta\tilde{n}} \frac{\sin[(l + \beta - \tilde{n})\pi]}{\sin[(l + \beta - \tilde{n})\pi/N]} - e^{j\theta\tilde{n}} \frac{\sin[(-l - \beta - \tilde{n})\pi]}{\sin[(-l - \beta - \tilde{n})\pi/N]} \right) + \mathbf{n}_\omega[\tilde{n}], \end{aligned} \quad (7)$$

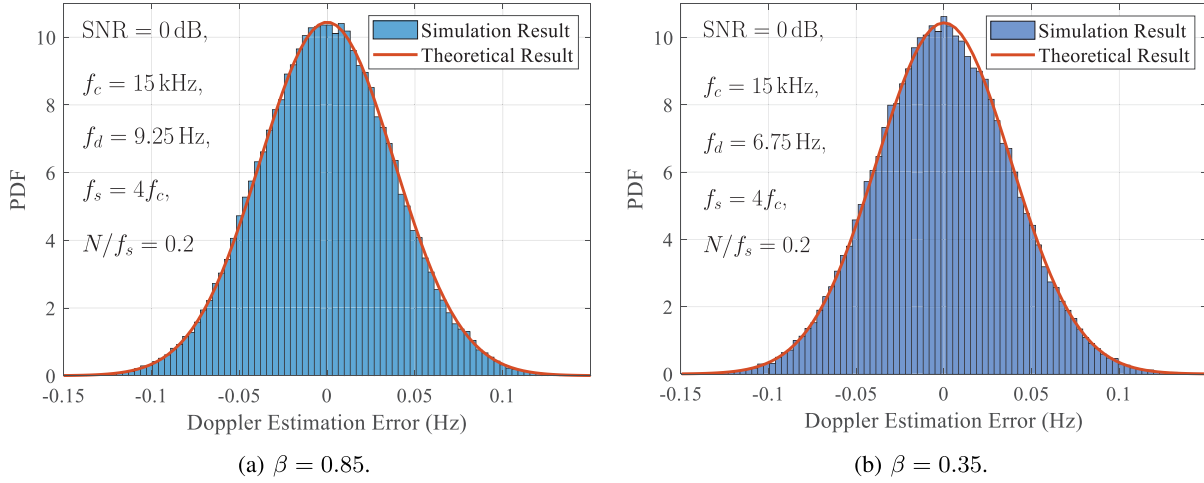


Fig. 4. The numerical and theoretical Doppler estimation error.

Based on (26), we can decide that the estimation error can be well approximated by the zero-mean Gaussian distribution. Similar to the analysis in previous section, we can obtain the variance of $\hat{\beta}_o$ as

$$\text{Var}\{\hat{\beta}_o\} = \frac{2\pi^2\sigma^2}{NA^2}(0.5 - \beta_o)^2(0.5 + \beta_o)^2 \cdot ((0.5 - \beta_o)^2 + (0.5 + \beta_o)^2). \quad (28)$$

The estimate of β will be

$$\hat{\beta} = \hat{\beta}_o - \lfloor \hat{\beta}_o \rfloor, \quad (29)$$

and the variance of $\hat{\beta}$ is

$$\text{var}\{\hat{\beta}\} = \text{var}\{\hat{\beta}_o\} = \frac{2\sigma^2 r_1(\beta)}{NA^2}, \quad (30)$$

where $r_1(\beta)$ is given in (31), shown at the bottom of the next page.

In Figure 3, for $\beta \in (0.25, 0.75)$, we have $r_0(\beta) < r_1(\beta)$. This means we should use (12) or (22) to estimate β . On the other hand, for $\beta \in [0, 0.25) \cup (0.75, 1)$, we have $r_0(\beta) > r_1(\beta)$. That is to say, (25) and (29) provide better estimate. As a result, after the estimation in the previous section, we need to decide if we should refine the results based on the method proposed in this section. To be specific, when $\hat{\beta} \in [0, 0.25) \cup (0.75, 1)$, we should re-estimate β based on (25) and (29).

The final expression of the variance of $\hat{\beta}$ will be

$$\text{var}\{\hat{\beta}\} \approx \frac{2\sigma^2}{NA^2}r(\beta), \quad (32)$$

where $r(\beta)$ is defined as

$$r(\beta) = \begin{cases} r_1(\beta) & \beta \in [0, 0.25) \cup [0.75, 1) \\ r_0(\beta) & \beta \in [0.25, 0.75]. \end{cases} \quad (33)$$

With $\hat{\beta}$, we have the estimate of f_d as $\hat{f}_d = f_s(l + \hat{\beta})/N - f_c$, and the variance is

$$\text{var}\{\hat{f}_d\} \approx \frac{f_s^2}{N^2} \cdot \text{var}\{\hat{\beta}\} \approx \frac{2\sigma^2 f_s^2}{N^3 A^2} r(\beta), \quad (34)$$

as is verified by the simulation results in Figure 4.

Apart from the Doppler shift, the amplitude of the received sequence can also be estimated by the least square (LS) method. For $\hat{\beta} \in [0, 0.5)$, the LS estimate of A is

$$\hat{A} = \frac{2\pi(1 - \hat{\beta})\hat{\beta}}{\sin(\hat{\beta}\pi)} \cdot \frac{(1 - \hat{\beta})|S_p| + \hat{\beta}|S_s|}{(1 - \hat{\beta})^2 + \hat{\beta}^2}. \quad (35)$$

For $\hat{\beta} \in [0.5, 1)$, we have the estimate of A as

$$\hat{A} = \frac{2\pi(1 - \hat{\beta})\hat{\beta}}{\sin(\hat{\beta}\pi)} \cdot \frac{(1 - \hat{\beta})|S_s| + \hat{\beta}|S_p|}{(1 - \hat{\beta})^2 + \hat{\beta}^2}. \quad (36)$$

\hat{A} can be used for SNR estimation, which is essential for the proposed algorithm in the following section. To be specific, different Doppler shift measurements have different accuracy due to different SNRs, and they should be assigned with different weights when they are employed for target localization.

III. DOPPLER-BASED LOCALIZATION

As has been discussed in [2] and [19], by employing the AUVs for underwater localization, better performance can be achieved at lower cost. In this section, we present a low-complexity AUV-aided localization system based on Doppler shift measurements.

A. System Description

With the onboard GPS and inertial sensors, the AUV can localize and synchronize itself [37], [38]. It moves around on the predefined trajectories and periodically broadcasts beacon signals, which contains two parts: the real-time three dimensional coordinate and velocity of the AUV, and a sinusoid wave at f_c Hz.¹ We assume that it moves on an arbitrary direction in constant velocity for several broadcast periods. Then, it alters the direction and follows the same procedure. This process will be repeated for M times, and the 3-dimensional velocity on

¹Although we are presenting the proposed system in the proactive mode, it can also work passively mode with very little configuration. To resolve the multi-target interference, different targets should work on different frequencies, which is totally possible because every target only consumes very narrow bandwidth.

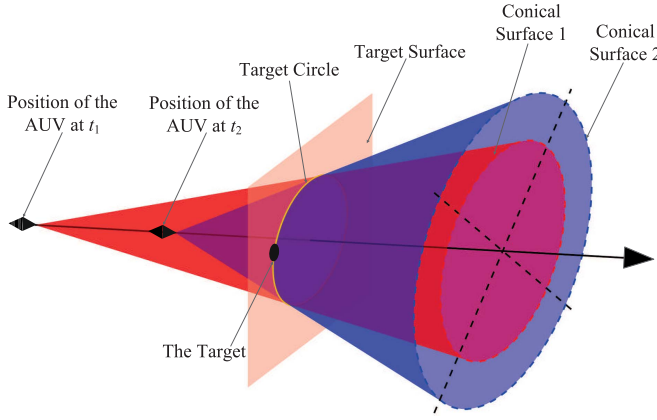


Fig. 5. Geometrical intuition of the low-complexity algorithm.

the m -th direction is $\mathbf{v}_m = [v_x^{(m)}, v_y^{(m)}, v_z^{(m)}]^T$. The position of the AUV at the k -th time slot on the m -th direction is $\mathbf{x}_{m,k} = [x_{m,k}, y_{m,k}, z_{m,k}]^T$, and the corresponding Doppler estimate is $f_D^{(m,k)}$.

Throughout this paper, we assume there is only one static target during the localization process. For a mobile target, multiple AUVs should be employed, and the target's velocity can be viewed as an extra unknown. Without loss of generality, we assume the position of the target device is $\mathbf{x} = [x, y, z]^T$. Then, let $d_{m,k} = |\mathbf{x} - \mathbf{x}_{m,k}|$, and we can obtain

$$\frac{(\mathbf{x} - \mathbf{x}_{m,k})^T \mathbf{v}_m}{d_{m,k}} \cdot \frac{f_c}{c} = f_D^{(m,k)}, \quad (37)$$

where c denotes the average underwater sound speed. This equation can be rearranged as

$$f_{m,k}(\theta) = \frac{(\mathbf{x}^T - \mathbf{x}_{m,k})^T \mathbf{v}_m}{d_{m,k}} \cdot \frac{f_c}{c} - f_D^{(m,k)} = 0, \quad (38)$$

where $\theta = [\mathbf{x}^T, c]^T$ contains the 3D coordinate of the target and the underwater acoustic velocity. Let $\mathbf{f}_m(\theta) = [f_{m,1}(\theta), f_{m,2}(\theta), \dots, f_{m,K}(\theta)]^T$ and we have

$$\mathbf{f}(\theta) = [\mathbf{f}_1(\theta)^T, \mathbf{f}_2(\theta)^T, \dots, \mathbf{f}_M(\theta)^T]^T. \quad (39)$$

By solving $\mathbf{f}(\theta) = \mathbf{0}$, the target's location can be estimated. It should be noted that the equations are formulated at the target side, which means the target needs to estimate the Doppler shifts. The target can obtain the real-time location information of the AUV by receiving the beacon messages. Generally, iterative algorithms can be employed to solve these nonlinear equations. However, the initial estimate should be carefully chosen to make sure the iterative algorithms converge. To avoid the initial estimation process, we propose a low-complexity two-phase algorithm in the following section.

B. The Proposed Low Complexity Algorithm

The proposed algorithm has two phases. In the first phase, the coarse localization result is obtained by extracting the linear constraints on the unknowns. However, because only the linear constraints are considered, we are not fully utilizing the information from the Doppler measurements. Therefore, we add a second phase, during which the localization result will be refined.

1) *Phase I: Coarse Localization:* As we have discussed, we want to extract the linear constraints on the target's location from the nonlinear equations. The intuition of the proposed method is presented in Figure 5. As we can see, the AUV moves on a straight line at a constant velocity. At t_1 , it broadcasts the beacon signal, and the target can decide that it is on a conical surface by estimating the Doppler shift. At t_2 , a second conical surface can be identified. The target must line on the intersection of these two conical surfaces, which is a circle, and that circle must lie on a specific plane. As long as we can find that plane, we can establish a linear equation with respect to the target's location. When the AUV moves in different directions, we can obtain a series of linear equations, by solving which the target's position can be estimated. We will unveil the mathematical details of the proposed method in the following discussions.

Assume that the AUV is moving on a line at a constant speed \mathbf{v}_m . We have two Doppler measurements $f_D^{(m,i)}$ and $f_D^{(m,j)}$, at the i -th and the j -th broadcast periods, respectively. Given that the positions of the AUV at these two periods are $\mathbf{x}_{m,i}$ and $\mathbf{x}_{m,j}$, the following equations can then be constructed

$$(\mathbf{x}^T - \mathbf{x}_{m,i}^T) \mathbf{v}_m = c_{m,i} d_{m,i}, \quad (40a)$$

$$(\mathbf{x}^T - \mathbf{x}_{m,j}^T) \mathbf{v}_m = c_{m,j} d_{m,j}, \quad (40b)$$

where $c_{m,i} = c f_D^{(m,i)} / f_c$ and $c_{m,j} = c f_D^{(m,j)} / f_c$. For (40a), we square both sides, and multiply them with $c_{m,j}^2$; for (40b), we square both sides and multiply them with $c_{m,i}^2$. We can then obtain

$$c_{m,j}^2 (\mathbf{x}^T \mathbf{v}_m - \mathbf{x}_{m,i}^T \mathbf{v}_m)^2 = c_{m,i}^2 c_{m,j}^2 |\mathbf{x} - \mathbf{x}_{m,i}|^2, \quad (41a)$$

$$c_{m,i}^2 (\mathbf{x}^T \mathbf{v}_m - \mathbf{x}_{m,j}^T \mathbf{v}_m)^2 = c_{m,i}^2 c_{m,j}^2 |\mathbf{x} - \mathbf{x}_{m,j}|^2. \quad (41b)$$

Subtract (41b) from (41a), leading to

$$c_{m,j}^2 (\mathbf{x}^T \mathbf{v}_m - \mathbf{x}_{m,i}^T \mathbf{v}_m)^2 - c_{m,i}^2 (\mathbf{x}^T \mathbf{v}_m - \mathbf{x}_{m,j}^T \mathbf{v}_m)^2 = c_{m,i}^2 c_{m,j}^2 (2\Delta T_{m,i,j} \mathbf{x}^T \mathbf{v}_m + |\mathbf{x}_{m,i}|^2 - |\mathbf{x}_{m,j}|^2), \quad (42)$$

where $\Delta T_{m,i,j}$ denotes the time lapse between the i -th and j -th time slots, and it satisfies $\mathbf{x}_{m,j} - \mathbf{x}_{m,i} = \Delta T_{m,i,j} \mathbf{v}_m$. Define $g_m = \mathbf{x}^T \mathbf{v}_m$, and we have

$$c_{m,j}^2 (g_m - \mathbf{x}_{m,i}^T \mathbf{v}_m)^2 - c_{m,i}^2 (g_m - \mathbf{x}_{m,j}^T \mathbf{v}_m)^2 = c_{m,i}^2 c_{m,j}^2 (2\Delta T_{m,i,j} g_m + |\mathbf{x}_{m,i}|^2 - |\mathbf{x}_{m,j}|^2). \quad (43)$$

$$r_1(\beta) = \begin{cases} \pi^2(0.5 - \beta)^2(0.5 + \beta)^2[(0.5 - \beta)^2 + (0.5 + \beta)^2] / \cos^2(\beta\pi), & \beta \in [0, 0.5) \\ \pi^2(0.5 - \beta)^2(1.5 - \beta)^2[(0.5 - \beta)^2 + (1.5 - \beta)^2] / \cos^2(\beta\pi), & \beta \in [0.5, 1) \end{cases} \quad (31)$$

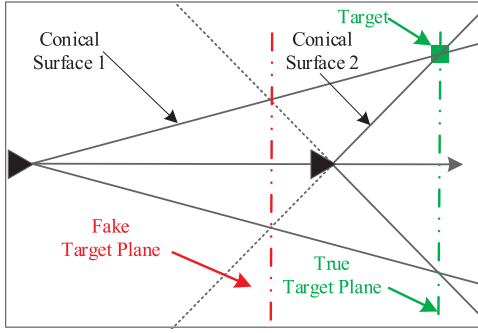


Fig. 6. The fake target plane and the true target plane.

(43) can be reorganized as

$$a_m g_m^2 + b_m g_m + c_m = 0, \quad (44)$$

where

$$\begin{aligned} a_m &= (c_{m,j}^2 - c_{m,i}^2), \\ b_m &= 2(-c_{m,j}^2 \mathbf{x}_{m,i}^T \mathbf{v}_m + c_{m,i}^2 \mathbf{x}_{m,j}^T \mathbf{v}_m \\ &\quad - c_{m,i}^2 c_{m,j}^2 \Delta T_{m,i,j}), \\ c_m &= c_{m,j}^2 (\mathbf{x}_{m,i}^T \mathbf{v}_m)^2 - c_{m,i}^2 (\mathbf{x}_{m,j}^T \mathbf{v}_m)^2 \\ &\quad + \Delta T_{m,i,j} c_{m,i}^2 c_{m,j}^2 (\mathbf{x}_{m,i} + \mathbf{x}_{m,j})^T \mathbf{v}_m. \end{aligned} \quad (45)$$

By solving (44), we will obtain two roots as

$$\hat{g}_m = \frac{-b_m \pm \sqrt{b_m^2 - 4a_m c_m}}{2a_m}. \quad (46)$$

These two roots represent two parallel planes, and the target can only lie on one of them. In Figure 6, we show these two planes in top view. As we can see, the intersection of two conical surfaces lies on the true target plane. However, if we extend the second conical surface to the opposite direction, it will have another intersection with the first conical surface, and that gives us the fake target plane. Mathematically, the fake solution originates from the squaring operations in (41a) and (41b). To identify the true target plane, we notice that g_m must satisfy the following inequality:

$$(g_m - \mathbf{x}_{m,k}^T \mathbf{v}_m) f_D^{(m,k)} = (g_m - \mathbf{x}_{m,k}^T \mathbf{v}_m)^2 f_c / d_{m,k} / c > 0, \quad (47)$$

where we implicitly replace $f_D^{(m,k)}$ with the left-hand-side of (37).

Note that we can use different combinations of $i, j \in \{1, 2, \dots, K\}$ to estimate g_m and average out noise. Assume we have obtained the valid solution as \hat{g}_m , and the target plane will be determined by $\mathbf{v}_m^T \mathbf{x} = \hat{g}_m$. This process will be repeated on M directions, and the following linear equation can be obtained $\mathbf{V} \mathbf{x} = \mathbf{g}$, where $\mathbf{g} = [\hat{g}_1, \hat{g}_2, \dots, \hat{g}_M]^T$ and $\mathbf{V} = [\mathbf{v}_1, \mathbf{v}_2, \dots, \mathbf{v}_M]^T$. We can then employ the least square estimator to obtain the coarse estimate of the target's location, given by

$$\hat{\mathbf{x}}_c = (\mathbf{V}^T \mathbf{V})^{-1} \mathbf{V}^T \mathbf{g}. \quad (48)$$

As we can see, the complexity of this algorithm grows linearly with the number of Doppler measurements. Also, it should

be noted that c is assumed to be known in this algorithm. Generally, it is not far away from 1500 m/s, and we can employ this value for the coarse estimation.

2) *Phase II: Refinement of the Result*: In Phase I, we are only partially using the information provided by the Doppler measurements. For example, in Figure 5, the Doppler estimates tell us that the target lies on a specific circle, but we are extending the searching area to a plane, which leads to information loss. As a result, we should find a way to further extract the available information and improve the localization accuracy.

The coarse estimate of $\boldsymbol{\theta}$ is $\hat{\boldsymbol{\theta}}_c = [\hat{\mathbf{x}}_c^T, \hat{c}_c]^T$, where $\hat{c}_c = 1500$ m/s. Let $\Delta\boldsymbol{\theta}$ be the estimation error caused by the inaccurate Doppler estimates, i.e., $\hat{\boldsymbol{\theta}}_c = \boldsymbol{\theta} + \Delta\boldsymbol{\theta}$. Because the Doppler estimation error is at the level of $1/N^3$, $\Delta\boldsymbol{\theta}$ can be well approximated by the first order Taylor expansion as

$$\mathbf{f}(\hat{\boldsymbol{\theta}}_c) - \mathbf{f}(\boldsymbol{\theta}) \approx \mathbf{H} \Delta\boldsymbol{\theta}. \quad (49)$$

\mathbf{H} is the Jacobian matrix given by

$$\mathbf{H} = \frac{\partial \mathbf{f}(\boldsymbol{\theta})}{\partial \boldsymbol{\theta}} = [\mathbf{H}_1^T, \mathbf{H}_2^T, \dots, \mathbf{H}_M^T]^T, \quad (50)$$

where \mathbf{H}_m is

$$\mathbf{H}_m = \begin{bmatrix} \frac{\partial f_{m,1}(\boldsymbol{\theta})}{\partial x} & \frac{\partial f_{m,1}(\boldsymbol{\theta})}{\partial y} & \frac{\partial f_{m,1}(\boldsymbol{\theta})}{\partial z} & \frac{\partial f_{m,1}(\boldsymbol{\theta})}{\partial c} \\ \frac{\partial f_{m,2}(\boldsymbol{\theta})}{\partial x} & \frac{\partial f_{m,2}(\boldsymbol{\theta})}{\partial y} & \frac{\partial f_{m,2}(\boldsymbol{\theta})}{\partial z} & \frac{\partial f_{m,2}(\boldsymbol{\theta})}{\partial c} \\ \vdots & \vdots & \vdots & \vdots \\ \frac{\partial f_{m,K}(\boldsymbol{\theta})}{\partial x} & \frac{\partial f_{m,K}(\boldsymbol{\theta})}{\partial y} & \frac{\partial f_{m,K}(\boldsymbol{\theta})}{\partial z} & \frac{\partial f_{m,K}(\boldsymbol{\theta})}{\partial c} \end{bmatrix}. \quad (51)$$

The partial derivatives in (51) are given by

$$\begin{aligned} \frac{\partial f_{m,k}(\boldsymbol{\theta})}{\partial x} &= \frac{f_c}{c} \cdot \left[\frac{v_x^{(m)}}{d_{m,k}} - \frac{(\mathbf{x} - \mathbf{x}_{m,k})^T \mathbf{v}_m (x - x_{m,k})}{d_{m,k}^3} \right] \\ \frac{\partial f_{m,k}(\boldsymbol{\theta})}{\partial y} &= \frac{f_c}{c} \cdot \left[\frac{v_y^{(m)}}{d_{m,k}} - \frac{(\mathbf{x} - \mathbf{x}_{m,k})^T \mathbf{v}_m (y - y_{m,k})}{d_{m,k}^3} \right] \\ \frac{\partial f_{m,k}(\boldsymbol{\theta})}{\partial z} &= \frac{f_c}{c} \cdot \left[\frac{v_z^{(m)}}{d_{m,k}} - \frac{(\mathbf{x} - \mathbf{x}_{m,k})^T \mathbf{v}_m (z - z_{m,k})}{d_{m,k}^3} \right] \\ \frac{\partial f_{m,k}(\boldsymbol{\theta})}{\partial c} &= -\frac{f_c}{c^2} \cdot \frac{(\mathbf{x} - \mathbf{x}_{m,k})^T \mathbf{v}_m}{d_{m,k}}. \end{aligned} \quad (52)$$

$\Delta\boldsymbol{\theta}$ can then be estimated with the weighted least square algorithm. However, \mathbf{H} is unavailable in practical scenarios, because $\boldsymbol{\theta}$ is unknown. As a result, we need to use $\mathbf{H}_c = \frac{\partial \mathbf{f}(\boldsymbol{\theta})}{\partial \boldsymbol{\theta}} \Big|_{\boldsymbol{\theta}=\hat{\boldsymbol{\theta}}_c}$ instead. Assume \mathbf{W} is the weighting matrix and the final result will be

$$\Delta\hat{\boldsymbol{\theta}} \approx (\mathbf{H}_c^T \mathbf{W} \mathbf{H}_c)^{-1} \mathbf{H}_c^T \mathbf{W} \mathbf{f}(\hat{\boldsymbol{\theta}}_c). \quad (53)$$

The next problem is how to choose the weighting matrix. Intuitively, if a Doppler measurement has a larger variance, the corresponding equation should be given a smaller weight. Therefore, we choose weights inversely proportional to the variances of Doppler estimates. Assume the amplitude of the received signal at the (m, k) -th time slot is $A_{m,k}$. Also, let $\omega_{m,k} = 2\pi(f_c + f_D^{(m,k)})/f_s$, and $\beta_{m,k} = \omega_{m,k}/\omega_0 - \lfloor \omega_{m,k}/\omega_0 \rfloor$, noting that these definitions are consistent with

those of ω and β in Section II. For the (m, k) -th Doppler estimate, the variance is

$$\sigma_{m,k}^2 = \frac{2f_s^2 \sigma^2}{N^3 A_{m,k}^2} \cdot r(\beta_{m,k}). \quad (54)$$

Because f_s , N and σ^2 are constant, the weight of the (m, k) -th equation can be defined as

$$w_{m,k} = \hat{A}_{m,k}^2 / r(\hat{\beta}_{m,k}), \quad (55)$$

where $\hat{A}_{m,k}$ and $\hat{\beta}_{m,k}$ are estimates of $A_{m,k}$ and $\beta_{m,k}$. With accurate estimates, we have the following approximation:

$$w_{m,k} \approx \frac{2f_s^2 \sigma^2}{N^3 \sigma_{m,k}^2}. \quad (56)$$

As we can see, $w_{m,k}$ is inversely proportional to the Doppler estimation variance of the received signals at the (m, k) -th time slot, and it is dependent on the amplitude and the fractional part of the normalized Doppler shift at that moment, as we have discussed in Section II. The weighting matrix can then be chosen as

$$\mathbf{W} = \text{diag}\{\mathbf{w}_1^T, \mathbf{w}_2^T, \dots, \mathbf{w}_M^T\}, \quad (57)$$

where $\mathbf{w}_m = [w_{m,1}, w_{m,2}, \dots, w_{m,K}]^T$. By using this weighting matrix, $|\mathbf{f}(\hat{\theta})|$ can be minimized. Due to space limit, we will not discuss this here, and the interested readers are referred to [39].

Then, the coarse estimate $\hat{\theta}_c$ can be refined as

$$\hat{\theta} = \hat{\theta}_c - \Delta \hat{\theta}. \quad (58)$$

The refined estimate of \mathbf{x} and c will be $\hat{\mathbf{x}} = \hat{\theta}[1 : 3]$ and $\hat{c} = \hat{\theta}[4]$, respectively. It should be noted that this process can be iterated to further improve the estimation accuracy. Based on our simulations, one or two iterations should be enough to provide very accurate localization results.

IV. PERFORMANCE ANALYSIS OF THE PROPOSED SYSTEM

A. Positioning Error of the Proposed System

Due to the estimation error in Doppler shifts, the localization error is inevitable. Assume \mathbf{f}_D contains the Doppler estimates and is defined as $\mathbf{f}_D = [\mathbf{f}_{D,1}^T, \mathbf{f}_{D,2}^T, \dots, \mathbf{f}_{D,M}^T]^T$, where $\mathbf{f}_{D,m}$ is given by

$$\mathbf{f}_{D,m} = [f_D^{(m,1)}, f_D^{(m,2)}, \dots, f_D^{(m,K)}]^T. \quad (59)$$

Let $\boldsymbol{\mu} = E\{\mathbf{f}_D|\boldsymbol{\theta}\}$ denote the accurate Doppler shifts, while $\boldsymbol{\Sigma} = E\{(\mathbf{f}_D - \boldsymbol{\mu})(\mathbf{f}_D - \boldsymbol{\mu})^T|\boldsymbol{\theta}\}$ gives the covariance matrix of \mathbf{f}_D . Generally, the estimation error of different Doppler shifts is independent, and $\boldsymbol{\Sigma}$ is a diagonal matrix. The Doppler estimation error vector will be $\mathbf{e}_f = \mathbf{f}_D - \boldsymbol{\mu}$, which leads to estimation error in $\hat{\theta}$. Employing (53) for refinement, the incurred estimation error in $\hat{\theta}$ can be approximately given by

$$\mathbf{e}_\theta \approx (\mathbf{H}^T \mathbf{W} \mathbf{H})^{-1} \mathbf{H}^T \mathbf{W} \mathbf{e}_f. \quad (60)$$

The covariance matrix of $\hat{\theta}$ is given by

$$\mathbf{R}_{\hat{\theta}} = E\{\mathbf{e}_\theta \mathbf{e}_\theta^T\}$$

$$\begin{aligned} &\approx E\{(\mathbf{H}^T \mathbf{W} \mathbf{H})^{-1} \mathbf{H}^T \mathbf{W} \mathbf{e}_f \mathbf{e}_f^T \mathbf{W} \mathbf{H} (\mathbf{H}^T \mathbf{W} \mathbf{H})^{-1}\} \\ &= (\mathbf{H}^T \mathbf{W} \mathbf{H})^{-1} \mathbf{H}^T \mathbf{W} E\{\mathbf{e}_f \mathbf{e}_f^T\} \mathbf{W} \mathbf{H} (\mathbf{H}^T \mathbf{W} \mathbf{H})^{-1} \\ &\approx (\mathbf{H}^T \boldsymbol{\Sigma} \mathbf{H})^{-1}, \end{aligned} \quad (61)$$

In the last step of (61), we implicitly employed the approximation $\mathbf{W} \approx 2\sigma^2 f_s^2 / N^3 \cdot \boldsymbol{\Sigma}^{-1}$. This is because the weighting factor of the (m, k) -th measurement is inversely proportional to the corresponding variance, as have been discussed in (56).

From another perspective, $\mathbf{R}_{\hat{\theta}}$ can also be written as

$$\mathbf{R}_{\hat{\theta}} = E\{\mathbf{e}_\theta \mathbf{e}_\theta^T\} = \begin{bmatrix} \mathbf{R}_{\hat{\mathbf{x}}} & \mathbf{R}_{\hat{\mathbf{x}}, \hat{c}} \\ \mathbf{R}_{\hat{\mathbf{x}}, \hat{c}}^T & R_{\hat{c}} \end{bmatrix}. \quad (62)$$

$\mathbf{R}_{\hat{\mathbf{x}}}$ is the covariance matrix of $\hat{\mathbf{x}}$, $R_{\hat{c}}$ is the variance of \hat{c} , and $\mathbf{R}_{\hat{\mathbf{x}}, \hat{c}} = E\{(\hat{\mathbf{x}} - \mathbf{x})(\hat{c} - c)\}$. The mean squared positioning error is $MSE\{\hat{\mathbf{x}}\} = \text{trace}\{\mathbf{R}_{\hat{\mathbf{x}}}\}$.

B. CRLB of the Proposed System

As we have demonstrated in Section II, the Doppler estimation error can be well approximated by zero-mean Gaussian distribution, and the variance is given by (34). In this section, we will derive the Fisher information matrix (FIM), which can be used to quantify the amount of the target's location information that can be extracted from the Doppler estimates.

To start with, the probability density function of \mathbf{f}_D is given by

$$p(\mathbf{f}_D|\boldsymbol{\theta}) = (2\pi)^{-MK/2} \cdot |\boldsymbol{\Sigma}|^{-1/2} \cdot \exp\left(-\frac{1}{2}(\mathbf{f}_D - \boldsymbol{\mu})^T \boldsymbol{\Sigma}^{-1}(\mathbf{f}_D - \boldsymbol{\mu})\right), \quad (63)$$

while its logarithm (i.e., $p_L(\mathbf{f}_D|\boldsymbol{\theta}) = \ln p(\mathbf{f}_D|\boldsymbol{\theta})$) is given by

$$l(\mathbf{f}_D|\boldsymbol{\theta}) = \frac{-NK}{2} \ln 2\pi - \frac{1}{2} \ln |\boldsymbol{\Sigma}| - \frac{1}{2}(\mathbf{f}_D - \boldsymbol{\mu})^T \boldsymbol{\Sigma}^{-1}(\mathbf{f}_D - \boldsymbol{\mu}). \quad (64)$$

Based on our analysis in Appendix VI, the FIM is given as

$$\mathbf{F} = \frac{\partial \boldsymbol{\mu}^T}{\partial \boldsymbol{\theta}} \boldsymbol{\Sigma}^{-1} \frac{\partial \boldsymbol{\mu}}{\partial \boldsymbol{\theta}} + \frac{1}{2} \left\{ \frac{\partial \boldsymbol{\sigma}^T}{\partial \boldsymbol{\theta}} \boldsymbol{\Sigma}^{-2} \frac{\partial \boldsymbol{\sigma}}{\partial \boldsymbol{\theta}} \right\}, \quad (65)$$

where $\boldsymbol{\sigma} = \text{diag}\{\boldsymbol{\Sigma}\}$. In Appendix VI, we have justified the following equations:

$$\frac{\partial \boldsymbol{\mu}}{\partial \boldsymbol{\theta}} = \mathbf{H}, \text{ and } \frac{\partial \boldsymbol{\sigma}}{\partial \boldsymbol{\theta}} = \mathbf{P} \mathbf{H}, \quad (66)$$

where $\mathbf{P} = \text{diag}([\mathbf{p}_1^T, \mathbf{p}_2^T, \dots, \mathbf{p}_M^T])$, and the k -th element of \mathbf{p}_m is given as

$$\mathbf{p}_m[k] = \frac{2f_s \sigma^2}{N^2 A_{m,k}^2} \cdot \frac{dr}{d\beta_{m,k}}. \quad (67)$$

Then, the FIM can be reorganized as

$$\begin{aligned} \mathbf{F} &= \mathbf{H}^T \boldsymbol{\Sigma}^{-1} \mathbf{H} + \frac{1}{2} \{ \mathbf{H}^T \mathbf{P} \boldsymbol{\Sigma}^{-2} \mathbf{P} \mathbf{H} \} \\ &= \mathbf{H}^T \left(\boldsymbol{\Sigma}^{-1} + \frac{1}{2} \mathbf{P} \boldsymbol{\Sigma}^{-2} \mathbf{P} \right) \mathbf{H}. \end{aligned} \quad (68)$$

The i -th diagonal element in Σ^{-1} corresponds to the (m, k) -th Doppler measurement, we have

$$\Sigma^{-1}[i, i] = \frac{N^3 A_{m,k}^2}{2f_s^2 \sigma^2 r(\beta_{m,k})} = \frac{NT_c^2 A_{m,k}^2}{2\sigma^2 r(\beta_{m,k})}, \quad (69)$$

where $T_c = N/f_s$ is the total sampling time. The i -th diagonal element in $\frac{1}{2}\mathbf{P}\Sigma^{-2}\mathbf{P}$ is

$$\begin{aligned} & \left(\frac{1}{2}\mathbf{P}\Sigma^{-2}\mathbf{P} \right) [l, l] \\ &= \left(\frac{2f_s^2 \sigma^2}{N^3 A_{m,k}^2} \cdot r(\beta_{m,k}) \right)^{-2} \left(\frac{2f_s \sigma^2}{N^2 A_{m,k}^2} \cdot \frac{dr}{d\beta_{m,k}} \right)^2 \\ &= \frac{T_c^2 (dr/d\beta_{m,k})^2}{2r^2(\beta_{m,k})}. \end{aligned} \quad (70)$$

As we can see, the i -th diagonal element in Σ^{-1} is proportional to N , while the corresponding value in $\frac{1}{2}\mathbf{P}\Sigma^{-2}\mathbf{P}$ is a constant. Generally, N is very large, which renders the second part negligible. Mathematically, we have the limit of \mathbf{F}/N as

$$\lim_{N \rightarrow \infty} \mathbf{F}/N = \mathbf{H}^T \Sigma_N^{-1} \mathbf{H}, \quad (71)$$

where $\Sigma_N = N\Sigma$. Or equivalently, the asymptotic FIM is

$$\mathbf{F} \sim \mathbf{H}^T \Sigma^{-1} \mathbf{H}. \quad (72)$$

This result is identical to the inverse of \mathbf{R}_θ in (61), which means the proposed algorithm can asymptotically achieve the CRLB. Although the result in (61) is only approximation by taking the first order Taylor expansion, it is actually very accurate, as will be shown in simulations.

C. Computational Complexity

The proposed algorithm contains three major steps. The first step is to estimate the Doppler shifts. The Doppler estimation algorithm in Section III involves the FFT, and the complexity is at the order of $\mathcal{O}\{N \log_2 N\}$. For MK measurements, the overall complexity is $\mathcal{O}\{MKN \log_2 N\}$. The second step is the coarse localization algorithm in Section IV.B. In (46), the computation complexity of calculating g_m 's is at the order of $\mathcal{O}\{MK\}$. In (48), the complexity of $\mathbf{V}^T \mathbf{V}$ is at the order of $\mathcal{O}\{M\}$, while that of matrix inversion is negligible, because it only involves a 3-dimensional matrix. In *Phase II*, the complexity of calculating the individual components is at the order of $\mathcal{O}\{MK\}$. To compute (55), the complexity is also at the level of $\mathcal{O}\{MK\}$. Generally, M and K are much smaller than N . As a result, the major computational complexity lies in the Doppler estimation, and thus, is at the order of $\mathcal{O}\{MKN \log_2 N\}$. To modern central processors, this complexity is acceptable even when N is very large. Besides, if we have some statistical information about the Doppler shifts, we do not need to compute the whole spectrum, and the FFT can be avoided. To be specific, we only need to analyze the spectrum for a specific frequency range, and the complexity can be reduced to the order of $\mathcal{O}\{MKN\}$.

V. NUMERICAL EVALUATIONS

In this section, we will conduct simulations to verify the analytical results in previous sections. To be specific, we will show that the approximated 3D positioning error is accurate and the asymptotic CRLB can be well approached. Also, we will show how different parameters contribute to the overall performance. As we have mentioned, multi-path components do not contribute to localization accuracy, and only the LoS component contains information regarding the target's position information. Therefore, the signal to noise ratio is defined as the signal strength over the combined strength of noise and the multi-path components inside the main lobe of the LoS signal. This is motivated by the fact that we are only using the main lobe of the LoS signal for Doppler estimation, and only the side lobes of reflected signals lying in the main lobe of the LoS signal have an impact on the Doppler estimation accuracy.

In the simulations, we assume there is only one target, and the target is static during the localization process. The system works in the proactive mode, which means the AUV keeps broadcasting its real-time location information and a sinusoid wave at a fixed frequency. f_c is set as 15 KHz, and sampling frequency is 60 KHz. Only the reflections from the sea surface is considered, because the target is assumed to lie on the seabed. The Doppler shift of the reflected path is simulated depending on the angle of arrival and the random fluctuation of the currents. The target is 500 meters below the sea surface. The AUV's velocity is 3 m/s, and the moving directions are randomly chosen. The beacon signals are broadcasted every 25 seconds, and the communication range is three kilometers. Initially, the AUV is deployed at the sea surface, and its horizontal distance to the target is 1500 meters. The reflected path is four times weaker than the LoS path. The average underwater velocity is assumed to be 1500 m/s, plus a zero-mean Gaussian variable, and the standard deviation is 10 m/s.

A. The Impact of Iteration Number and SNR

As we have briefly mentioned in Section III-B, if we repeat the refinement process in *Phase II*, the localization accuracy can be improved. Simulations are conducted and the results are presented in Figure 7. The sampling time is fixed as 0.1 s, and the AUV moves on five different directions and broadcasts two beacon signals on every direction. When the iteration number (N_{iter}) equals zero, there is a discernable gap between the CRLB and the MSE of the proposed method, especially in low SNR regime. However, by adding one iteration, the localization accuracy can be substantially improved. When the iteration number increases to 2 or 3, the localization error will decrease continuously, but the performance gain is negligible. As a result, the iteration number will be chosen as four for the remaining simulations. Also, we notice that as SNR increases, localization error decreases consistently, because Doppler shift can be more accurately estimated. As a matter of fact, the variance of 3D localization error is inversely proportional to the SNR, as we can observe in (61). From the results in Fig. 7, and also from Fig. 8 and 9, we can see that

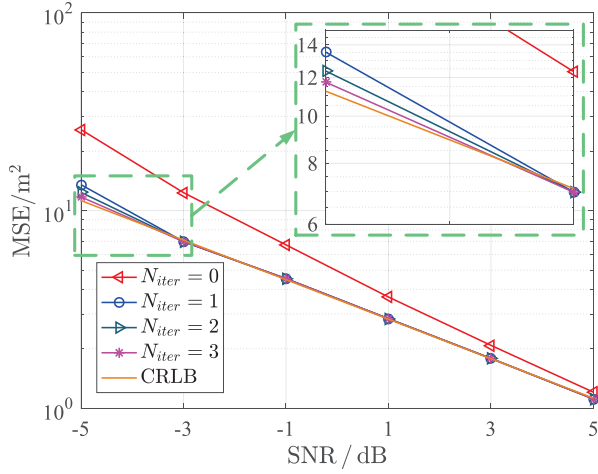
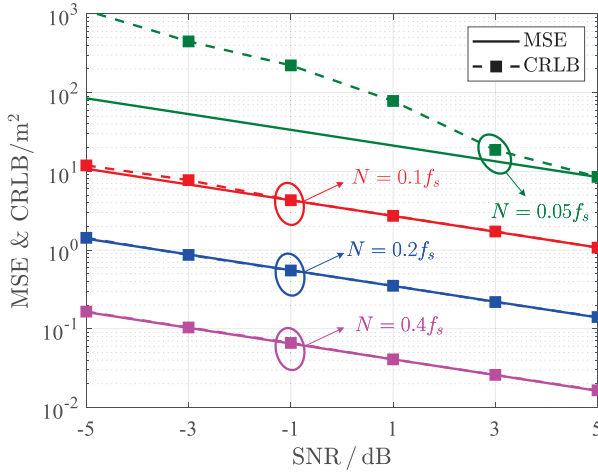


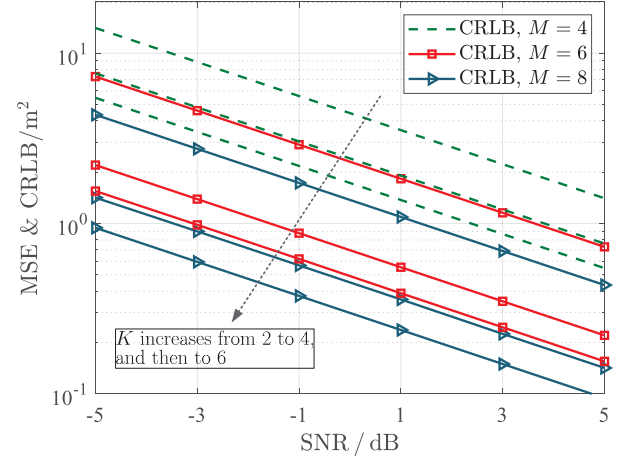
Fig. 7. The impact of iteration number and SNR on localization accuracy.

Fig. 8. The impact of N on localization accuracy.

the approximation in (60) is very accurate, which indicates the accuracy of (49).

B. The Impact of N and SNR

Intuitively, as we increase N or SNR, the accuracy of Doppler estimation will be improved. As a result, localization accuracy should be improved. In this section, we will evaluate the system performance for different N and SNR values. Because the sampling frequency is fixed, the increase of N is equivalent to the increase of sampling time. The simulation results are presented in Figure 8. Every time we double the number of samples, the MSE of localization result will be reduced by a factor of 8, which is consistent with our analysis. Moreover, we notice that for $N = 0.05f_s$, the proposed algorithm has a significant performance gap compared to CRLB. This is because our analysis is based on the first order Taylor expansion, which is only accurate for small Doppler shift estimation error. However, when N is not large enough, Doppler estimation error will be significant and the result in (34) is no longer accurate.

Fig. 9. The impact of M and K on localization accuracy.

C. The impact of M and K

When we increase M and K , the localization error is expected to decrease. In this section, we conduct simulations for different combinations of M and K . The results are shown in Figure 9. As we can see, K is increased from 2 to 4, and then to 6, while M varies in $\{4, 6, 8\}$. Generally, by increasing M and K , more measurements can be obtained, and better localization accuracy can be achieved. However, the impact is more complicated compared to that of N . As has been pointed out by many researchers, the trajectory of the AUV has a significant impact on the localization accuracy. Therefore, depending on the trajectory of the AUV, the increase of M and K may show significant or negligible influence on performance.

VI. CONCLUSION

In this paper, we propose an AUV-aided underwater localization system, and Doppler shift is employed as the metric. The major work lies in two aspects: Doppler estimation error analysis and low-complexity algorithm design. For the Doppler estimation, a conventional low-complexity algorithm is employed and a simple method has been proposed to improve the accuracy. Also, the estimation error is thoroughly analyzed for both the original and refined algorithms. Based on the Doppler estimates, a series of nonlinear equations are obtained, and a two-phase linear algorithm is proposed to solve them. The positioning error of this system has been analyzed, and the closed-form results are obtained. Moreover, the CRLB of the proposed system is discussed. We also show that the proposed linear algorithm can asymptotically achieve the CRLB. Last but not the least, simulations are conducted to verify the theoretical analysis, and evaluate the impacts of different parameters.

APPENDIX A STATISTICS OF \mathbf{n}_ω

The covariance matrix of \mathbf{n}_ω is $E\{\mathbf{n}_\omega \mathbf{n}_\omega^H\} = \sigma^2/N \cdot \mathbf{I}_N$. For any element in \mathbf{n}_ω , the real and imaginary parts have an

identical variance of $\frac{\sigma^2}{2N}$. The real part of $\mathbf{n}_\omega[k]$ is

$$\Re\{\mathbf{n}_\omega[\tilde{n}]\} = \frac{1}{N} \sum_{n=0}^{N-1} \mathbf{n}_s[n] \cos(\tilde{n}n\omega_0), \quad (73)$$

while the imaginary part is

$$\Im\{\mathbf{n}_\omega[\tilde{n}]\} = \frac{1}{N} \sum_{n=0}^{N-1} \mathbf{n}_s[n] \sin(\tilde{n}n\omega_0). \quad (74)$$

We can prove that they are uncorrelated:

$$\begin{aligned} E\{\Re\{\mathbf{n}_\omega[\tilde{n}]\}\Im\{\mathbf{n}_\omega[\tilde{n}]\}\} \\ = \frac{1}{N^2} \sum_{n_1=0}^{N-1} \sum_{n_2=0}^{N-1} E\{\mathbf{n}_s[n_1]\mathbf{n}_s[n_2]\} \cos(\tilde{n}n_1\omega_0) \sin(\tilde{n}n_2\omega_0) \\ = \frac{1}{N^2} \sum_{n=0}^{N-1} \sigma^2 \cos(\tilde{n}n\omega_0) \sin(\tilde{n}n\omega_0) = 0. \end{aligned} \quad (75)$$

Similarly, for any two elements in \mathbf{n}_ω (e.g., $\mathbf{n}_\omega[\tilde{n}_1]$ and $\mathbf{n}_\omega[\tilde{n}_2]$, $\tilde{n}_1 \neq \tilde{n}_2$), we can prove that

$$\begin{aligned} E\{\Re\{\mathbf{n}_\omega[\tilde{n}_1]\}\Im\{\mathbf{n}_\omega[\tilde{n}_2]\}\} \\ = E\{\Re\{\mathbf{n}_\omega[\tilde{n}_1]\}\Re\{\mathbf{n}_\omega[\tilde{n}_2]\}\} \\ = E\{\Im\{\mathbf{n}_\omega[\tilde{n}_1]\}\Im\{\mathbf{n}_\omega[\tilde{n}_2]\}\} = 0. \end{aligned} \quad (76)$$

APPENDIX B PROOF OF CRLB IN (65)

Define θ_p as the p -th element in $\boldsymbol{\theta}$, i.e., $\theta_p = \boldsymbol{\theta}[p]$. The partial derivative of $p_L(\mathbf{f}_D|\mathbf{x}, c)$, with respect to θ_p is given in (77), shown at the top of the next page. As we can see, $\frac{\partial p_L}{\partial \theta_p}$ contains three components, $B_{p,1}$, $B_{p,2}$, and $B_{p,3}$. The (p, q) -th element in \mathbf{F} is

$$\mathbf{F}[p, q] = E\left\{\frac{\partial p_L}{\partial \theta_p} \cdot \frac{\partial p_L}{\partial \theta_q}\right\} = \frac{1}{4} E\left\{\sum_{i=1}^3 \sum_{j=1}^3 B_{p,i} B_{q,j}\right\}. \quad (78)$$

We have

$$\begin{aligned} E\{B_{p,1}B_{q,1}\} &= 4 \frac{\partial \boldsymbol{\mu}^T}{\partial \theta_p} \boldsymbol{\Sigma}^{-1} \frac{\partial \boldsymbol{\mu}}{\partial \theta_q} \\ E\{B_{p,1}B_{q,2}\} &= E\{B_{p,1}B_{q,3}\} = 0 \\ E\{B_{p,2}B_{q,3}\} &= B_{p,3}E\{B_{q,2}\} \\ &= -\text{trace}\left\{\boldsymbol{\Sigma}^{-1} \frac{\partial \boldsymbol{\Sigma}}{\partial \theta_p}\right\} \text{trace}\left\{\boldsymbol{\Sigma}^{-1} \frac{\partial \boldsymbol{\Sigma}}{\partial \theta_q}\right\} \\ E\{B_{p,3}B_{q,3}\} &= B_{p,3}B_{q,3} \\ &= \text{trace}\left\{\boldsymbol{\Sigma}^{-1} \frac{\partial \boldsymbol{\Sigma}}{\partial \theta_p}\right\} \text{trace}\left\{\boldsymbol{\Sigma}^{-1} \frac{\partial \boldsymbol{\Sigma}}{\partial \theta_q}\right\}, \end{aligned} \quad (79)$$

and $E\{B_{p,2}B_{q,2}\}$ is derived in (80), shown at the top of the next page. Therefore, $\mathbf{F}[p, q]$ is given by

$$\mathbf{F}[p, q] = \frac{\partial \boldsymbol{\mu}^T}{\partial \theta_p} \boldsymbol{\Sigma}^{-1} \frac{\partial \boldsymbol{\mu}}{\partial \theta_q} + \frac{1}{2} \left\{ \frac{\partial \boldsymbol{\sigma}^T}{\partial \theta_p} \boldsymbol{\Sigma}^{-2} \frac{\partial \boldsymbol{\sigma}}{\partial \theta_q} \right\}, \quad (81)$$

where we implicitly use the fact that $\frac{\partial \boldsymbol{\Sigma}^{-1}}{\partial \theta_p} = -\boldsymbol{\Sigma}^{-2} \frac{\partial \boldsymbol{\Sigma}}{\partial \theta_p}$, and $B_{p,3} = \text{trace}\left\{\boldsymbol{\Sigma}^{-1} \frac{\partial \boldsymbol{\Sigma}}{\partial \theta_p}\right\}$. (81) can then be reorganized as (65).

APPENDIX C PROOF OF (66)

Let $\boldsymbol{\mu}_m = [\mu_{m,1}, \mu_{m,2}, \dots, \mu_{m,K}]^T$, and we have $\boldsymbol{\mu} = [\boldsymbol{\mu}_1^T, \boldsymbol{\mu}_2^T, \dots, \boldsymbol{\mu}_M^T]^T$, where $\mu_{m,k}$ is given as

$$\mu_{m,k} = E\{f_D^{(m,k)}|\mathbf{x}, c\} = \frac{(\mathbf{x} - \mathbf{x}_{m,k})^T \mathbf{v}_m}{d_{m,k}} \cdot \frac{f_c}{c}. \quad (82)$$

As a result, we have

$$\frac{\partial \boldsymbol{\mu}}{\partial \boldsymbol{\theta}} = \mathbf{H}. \quad (83)$$

The partial derivative of $\sigma_{m,k}^2$ with respect to $\boldsymbol{\theta}$ is

$$\begin{aligned} \frac{\partial \sigma_{m,k}^2}{\partial \boldsymbol{\theta}} &= \frac{2f_s^2 \sigma^2}{N^3 A_{m,k}^2} \cdot \frac{dr}{d\beta_{m,k}} \cdot \frac{\partial \beta_{m,k}}{\partial \boldsymbol{\theta}} \\ &= \frac{2f_s \sigma^2}{N^2 A_{m,k}^2} \cdot \frac{dr}{d\beta_{m,k}} \cdot \frac{\partial f_{m,k}(\boldsymbol{\theta})}{\partial \boldsymbol{\theta}}. \end{aligned} \quad (84)$$

$dr/d\beta$ is given by

$$\frac{dr}{d\beta} = \begin{cases} \frac{[\tilde{a}_1(\beta) \cos^2(\beta\pi) + \tilde{b}_1(\beta)\pi \sin(2\beta\pi)] \pi^2}{\cos^4(\beta\pi)} & \beta \in [0, 0.25) \\ \frac{[\tilde{a}_2(\beta) \sin^2(\beta\pi) + \tilde{b}_2(\beta)\pi \sin(2\beta\pi)] \pi^2}{\sin^4(\beta\pi)} & \beta \in (0.25, 0.75) \\ \frac{[\tilde{a}_3(\beta) \cos^2(\beta\pi) + \tilde{b}_3(\beta)\pi \sin(2\beta\pi)] \pi^2}{\cos^4(\beta\pi)} & \beta \in (0.75, 1). \end{cases} \quad (85)$$

where we have

$$\begin{aligned} \tilde{a}_1(\beta) &= (2\beta^2 - 0.5)(6\beta^3 + 0.5\beta) \\ \tilde{b}_1(\beta) &= (\beta^2 - 0.25)^2(2\beta^2 + 0.5) \\ \tilde{a}_2(\beta) &= 2(1 - 2\beta)(3\beta^2 - 3\beta + 1)\beta(1 - \beta) \\ \tilde{b}_2(\beta) &= -(2\beta^2 - 2\beta + 1)(\beta^2 - \beta)^2 \\ \tilde{a}_3(\beta) &= (\beta - 1)(2\beta^2 - 4\beta + 1.5)(6\beta^2 - 12\beta + 6.5) \\ \tilde{b}_3(\beta) &= (\beta^2 - 2\beta + 0.75)^2(2\beta^2 - 4\beta + 3.25). \end{aligned} \quad (86)$$

Because

$$\beta_{m,k} = (f_c + f_D^{(m,k)})N/f_s - [(f_c + f_D^{(m,k)})N/f_s], \quad (87)$$

we have

$$\frac{\partial \beta_{m,k}}{\partial \boldsymbol{\theta}} = \frac{N}{f_s} \cdot \frac{\partial f_{m,k}(\boldsymbol{\theta})}{\partial \boldsymbol{\theta}}. \quad (88)$$

Let $\mathbf{p} = [\mathbf{p}_1^T, \mathbf{p}_2^T, \dots, \mathbf{p}_M^T]^T$, and the k -th element of \mathbf{p}_m is given as

$$\mathbf{p}_m[k] = \frac{2f_s \sigma^2}{N^2 A_{m,k}^2} \cdot \frac{dr}{d\beta_{m,k}}. \quad (89)$$

Then, we can organize the results and conclude

$$\frac{\partial \boldsymbol{\sigma}}{\partial \boldsymbol{\theta}} = \mathbf{P}\mathbf{H}, \quad (90)$$

where $\mathbf{P} = \text{diag}(\mathbf{p})$.

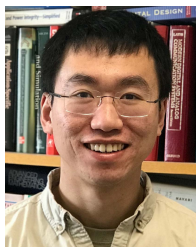
$$\begin{aligned}
\frac{\partial p_L}{\partial \theta_p} &= -\frac{1}{2} \left(\frac{\partial \boldsymbol{\mu}^T}{\partial \theta_p} \boldsymbol{\Sigma}^{-1} (\boldsymbol{\mu} - \mathbf{f}_D) + (\boldsymbol{\mu} - \mathbf{f}_D)^T \left(\frac{\partial \boldsymbol{\Sigma}^{-1}}{\partial \theta_p} (\boldsymbol{\mu} - \mathbf{f}_D) + \boldsymbol{\Sigma}^{-1} \frac{\partial \boldsymbol{\mu}}{\partial \theta_p} \right) + \frac{\partial \ln |\boldsymbol{\Sigma}|}{\partial \theta_p} \right) \\
&= -\underbrace{\frac{\partial \boldsymbol{\mu}^T}{\partial \theta_p} \boldsymbol{\Sigma}^{-1} (\boldsymbol{\mu} - \mathbf{f}_D)}_{B_{p,1}} - \underbrace{\frac{1}{2} (\boldsymbol{\mu} - \mathbf{f}_D)^T \frac{\partial \boldsymbol{\Sigma}^{-1}}{\partial \theta_p} (\boldsymbol{\mu} - \mathbf{f}_D)}_{B_{p,2}} - \underbrace{\frac{1}{2} \frac{\partial \ln |\boldsymbol{\Sigma}|}{\partial \theta_p}}_{B_{p,3}}
\end{aligned} \tag{77}$$

$$\begin{aligned}
E\{B_{p,2}B_{q,2}\} &= E\left\{(\boldsymbol{\mu} - \mathbf{f}_D)^T \frac{\partial \boldsymbol{\Sigma}^{-1}}{\partial \theta_p} (\boldsymbol{\mu} - \mathbf{f}_D) (\boldsymbol{\mu} - \mathbf{f}_D)^T \frac{\partial \boldsymbol{\Sigma}^{-1}}{\partial \theta_q} (\boldsymbol{\mu} - \mathbf{f}_D)\right\} \\
&= \text{diag}\left\{\boldsymbol{\Sigma}^{-2} \frac{\partial \boldsymbol{\Sigma}}{\partial \theta_p}\right\} (\boldsymbol{\sigma} \boldsymbol{\sigma}^T + 2\boldsymbol{\Sigma}^2) \text{diag}\left\{\boldsymbol{\Sigma}^{-2} \frac{\partial \boldsymbol{\Sigma}}{\partial \theta_q}\right\} \\
&= \text{diag}\left\{\boldsymbol{\Sigma}^{-2} \frac{\partial \boldsymbol{\Sigma}}{\partial \theta_p}\right\} \boldsymbol{\sigma} \boldsymbol{\sigma}^T \text{diag}\left\{\boldsymbol{\Sigma}^{-2} \frac{\partial \boldsymbol{\Sigma}}{\partial \theta_q}\right\} + 2 \text{diag}\left\{\boldsymbol{\Sigma}^{-2} \frac{\partial \boldsymbol{\Sigma}}{\partial \theta_p}\right\} \boldsymbol{\Sigma}^2 \text{diag}\left\{\boldsymbol{\Sigma}^{-2} \frac{\partial \boldsymbol{\Sigma}}{\partial \theta_q}\right\} \\
&= \text{trace}\left\{\boldsymbol{\Sigma}^{-1} \frac{\partial \boldsymbol{\Sigma}}{\partial \theta_p}\right\} \text{trace}\left\{\boldsymbol{\Sigma}^{-1} \frac{\partial \boldsymbol{\Sigma}}{\partial \theta_q}\right\} + 2 \text{trace}\left\{\frac{\partial \boldsymbol{\Sigma}}{\partial \theta_p} \boldsymbol{\Sigma}^{-2} \frac{\partial \boldsymbol{\Sigma}}{\partial \theta_q}\right\} \\
&= \text{trace}\left\{\boldsymbol{\Sigma}^{-1} \frac{\partial \boldsymbol{\Sigma}}{\partial \theta_p}\right\} \text{trace}\left\{\boldsymbol{\Sigma}^{-1} \frac{\partial \boldsymbol{\Sigma}}{\partial \theta_q}\right\} + 2 \left\{\frac{\partial \boldsymbol{\sigma}^T}{\partial \theta_p} \boldsymbol{\Sigma}^{-2} \frac{\partial \boldsymbol{\sigma}}{\partial \theta_q}\right\}
\end{aligned} \tag{80}$$

REFERENCES

- [1] M. Isik and O. Akan, "A three dimensional localization algorithm for underwater acoustic sensor networks," *IEEE Trans. Wireless Commun.*, vol. 8, no. 9, pp. 4457–4463, Sep. 2009.
- [2] Z. Gong *et al.*, "Design, analysis, and field testing of an innovative drone-assisted zero-configuration localization framework for wireless sensor networks," *IEEE Trans. Veh. Technol.*, vol. 66, no. 11, pp. 10322–10335, Nov. 2017.
- [3] B. Zhou, Q. Chen, and P. Xiao, "The error propagation analysis of the received signal strength-based simultaneous localization and tracking in wireless sensor networks," *IEEE Trans. Inf. Theory*, vol. 63, no. 6, pp. 3983–4007, Jun. 2017.
- [4] Y. Shen and M. Z. Win, "Fundamental limits of wideband localization—Part I: A general framework," *IEEE Trans. Inf. Theory*, vol. 56, no. 10, pp. 4956–4980, Oct. 2010.
- [5] Y. Shen, H. Wymeersch, and M. Z. Win, "Fundamental limits of wideband localization—Part II: Cooperative networks," *IEEE Trans. Inf. Theory*, vol. 56, no. 10, pp. 4981–5000, Oct. 2010.
- [6] M. Erol, L. F. M. Vieira, and M. Gerla, "AUV-Aided Localization for Underwater Sensor Networks," in *Proc. Int. Conf. Wireless Algorithms, Syst. Appl. (WASA)*, Aug. 2007.
- [7] D. Mirza and C. Schurgers, "Collaborative localization for fleets of underwater drifters," in *Proc. OCEANS*, Vancouver, BC, Canada, Sep. 2007, pp. 1–6.
- [8] M. Waldmeyer, H.-P. Tan, and W. K. Seah, "Multi-stage AUV-aided localization for underwater wireless sensor networks," in *Proc. IEEE Workshops Int. Conf. Adv. Inf. Netw. Appl.*, Mar. 2011, pp. 908–913.
- [9] R. Zandi, M. Kamarei, and H. Amiri, "Underwater acoustic sensor network localization using four directional beams," in *Proc. 21st Iranian Conf. Electr. Eng. (ICEE)*, May 2013, pp. 1–6.
- [10] H. Maqsood, N. Javaid, A. Yahya, B. Ali, Z. A. Khan, and U. Qasim, "Mobil-AUV: AUV-aided localization scheme for underwater wireless sensor networks," in *Proc. 10th Int. Conf. Innov. Mobile Internet Services Ubiquitous Comput. (IMIS)*, Jul. 2016, pp. 170–175.
- [11] R. Diamant and L. Lampe, "Underwater localization with time-synchronization and propagation speed uncertainties," *IEEE Trans. Mobile Comput.*, vol. 12, no. 7, pp. 1257–1269, Jul. 2013.
- [12] D. M. Crimmins *et al.*, "Long-endurance test results of the solar-powered AUV system," in *Proc. OCEANS*, Boston, MA, USA, Sep. 2006, pp. 1–5.
- [13] B. Ferreira, M. Pinto, A. Matos, and N. Cruz, "Modeling and motion analysis of the mares autonomous underwater vehicle," in *Proc. OCEANS*, Oct. 2009, pp. 1–10.
- [14] G. Han, J. Jiang, L. Shu, Y. Xu, and F. Wang, "Localization algorithms of underwater wireless sensor networks: A survey," *Sensors*, vol. 12, no. 2, pp. 2026–2061, Feb. 2012.
- [15] Q. Liang, B. Zhang, C. Zhao, and Y. Pi, "TDoA for passive localization: Underwater versus terrestrial environment," *IEEE Trans. Parallel Distrib. Syst.*, vol. 24, no. 10, pp. 2100–2108, Oct. 2013.
- [16] J. Liu, Z. Wang, J.-H. Cui, S. Zhou, and B. Yang, "A joint time synchronization and localization design for mobile underwater sensor networks," *IEEE Trans. Mobile Comput.*, vol. 15, no. 3, pp. 530–543, Mar. 2016.
- [17] W. Burdick, *Underwater Acoustic System Analysis*. Newport Beach, CA, USA: Peninsula Publishing, 2002.
- [18] J. Zheng, K. W. Lui, and H. So, "Accurate three-step algorithm for joint source position and propagation speed estimation," *Signal Process.*, vol. 87, no. 12, pp. 3096–3100, Dec. 2007.
- [19] Z. Gong, C. Li, and F. Jiang, "AUV-aided joint localization and time synchronization for underwater acoustic sensor networks," *IEEE Signal Process. Lett.*, vol. 25, no. 4, pp. 477–481, Apr. 2018.
- [20] J. Zheng and Y.-C. Wu, "Joint time synchronization and localization of an unknown node in wireless sensor networks," *IEEE Trans. Signal Process.*, vol. 58, no. 3, pp. 1309–1320, Mar. 2010.
- [21] D. Park, K. Kwak, W. K. Chung, and J. Kim, "Development of underwater short-range sensor using electromagnetic wave attenuation," *IEEE J. Ocean. Eng.*, vol. 41, no. 2, pp. 318–325, Apr. 2016.
- [22] P. De Theije and J.-C. Sindt, "Single-ping target speed and course estimation using a bistatic sonar," *IEEE J. Ocean. Eng.*, vol. 31, no. 1, pp. 236–243, Jan. 2006.
- [23] R. Diamant, L. M. Wolff, and L. Lampe, "Location tracking of ocean-current-related underwater drifting nodes using doppler shift measurements," *IEEE J. Ocean. Eng.*, vol. 40, no. 4, pp. 887–902, Oct. 2015.
- [24] D. J. Peters, "A Bayesian method for localization by multistatic active sonar," *IEEE J. Ocean. Eng.*, vol. 42, no. 1, pp. 135–142, Jan. 2017.
- [25] P. Carroll, K. Domrese, H. Zhou, S. Zhou, and P. Willett, "Doppler-aided localization of mobile nodes in an underwater distributed antenna system," *Phys. Commun.*, vol. 18, pp. 49–59, Mar. 2016.
- [26] R. Spindel, R. Porter, W. Marquet, and J. Durham, "A high-resolution pulse-Doppler underwater acoustic navigation system," *IEEE J. Ocean. Eng.*, vol. JOE-1, no. 1, pp. 6–13, Sep. 1976.
- [27] C. Berger, S. Zhou, J. Preisig, and P. Willett, "Sparse channel estimation for multicarrier underwater acoustic communication: From subspace methods to compressed sensing," in *Proc. OCEANS-EUROPE*, Bremen, Germany, May 2009, pp. 1–8.
- [28] Y. Zhao, H. Yu, G. Wei, F. Ji, and F. Chen, "Parameter estimation of wideband underwater acoustic multipath channels based on fractional fourier transform," *IEEE Trans. Signal Process.*, vol. 64, no. 20, pp. 5396–5408, Oct. 2016.
- [29] B. Li, S. Zhou, M. Stojanovic, L. Freitag, and P. Willett, "Multicarrier communication over underwater acoustic channels with nonuniform Doppler shifts," *IEEE J. Ocean. Eng.*, vol. 33, no. 2, pp. 198–209, Apr. 2008.

- [30] T. Xu, Z. Tang, G. Leus, and U. Mitra, "Multi-rate block transmission over wideband multi-scale multi-lag channels," *IEEE Trans. Signal Process.*, vol. 61, no. 4, pp. 964–979, Feb. 2013.
- [31] M. Stojanovic and J. Preisig, "Underwater acoustic communication channels: Propagation models and statistical characterization," *IEEE Commun. Mag.*, vol. 47, no. 1, pp. 84–89, Jan. 2009.
- [32] Y. Zhang, Y. Huang, L. Wan, S. Zhou, X. Shen, and H. Wang, "Adaptive OFDMA with partial CSI for downlink underwater acoustic communications," *J. Commun. Netw.*, vol. 18, no. 3, pp. 387–396, Jun. 2016.
- [33] R. P. Porter, R. C. Spindel, and R. J. Jaffee, "CW beacon system for hydrophone motion determination," *J. Acoust. Soc. Amer.*, vol. 53, no. 6, pp. 1691–1699, Jun. 1973.
- [34] S. Mason, C. Berger, S. Zhou, and P. Willett, "Detection, synchronization, and Doppler scale estimation with multicarrier waveforms in underwater acoustic communication," *IEEE J. Sel. Areas Commun.*, vol. 26, no. 9, pp. 1638–1649, Dec. 2008.
- [35] F. Qu, Z. Wang, L. Yang, and Z. Wu, "A journey toward modeling and resolving Doppler in underwater acoustic communications," *IEEE Commun. Mag.*, vol. 54, no. 2, pp. 49–55, Feb. 2016.
- [36] Z. Gong, C. Li, and F. Jiang, "Analysis of the multi-path effect in underwater Doppler estimation accuracy," *IEEE Commun. Lett.*, to be published. [Online]. Available: <http://www.engr.mun.ca/~licheng/publications.html>
- [37] G. T. Donovan, "Position error correction for an autonomous underwater vehicle inertial navigation system (INS) using a particle filter," *IEEE J. Ocean. Eng.*, vol. 37, no. 3, pp. 431–445, Jul. 2012.
- [38] C. M. Lee, S. W. H. P. M. Lee, S. M. Kim, and W. Seong, "Underwater navigation Doppler velocity log using indirect feedback Kalman filter," *J. Ocean Eng. Technol.*, vol. 6, no. 6, Jan. 2004.
- [39] T. Strutz, *Data Fitting Uncertainty: A Practical Introduction to Weighted Least Squares Beyond*. Germany: Vieweg and Teubner, 2010.



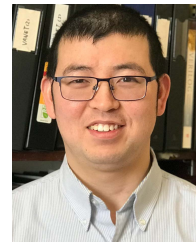
Zijun Gong received the B.Eng. and M.Eng. degrees from the Harbin Institute of Technology (HIT), Harbin, China, in 2013 and 2015, respectively. He is currently pursuing the Ph.D. degree with the Memorial University of Newfoundland (MUN), St. John's, NL, Canada. His research interests include WLAN fingerprint-based indoor localization systems, radio propagation modeling, localization of WSN, and localization of underwater vehicles. Also, he did some research on channel estimation in massive MIMO, and millimeter wave communications.

He received the Best Paper Award at the 2017 IEEE Global Telecommunications Conference (Globecom'17), Singapore, December 2017.



Cheng Li (Senior Member, IEEE) received the B.Eng. and M.Eng. degrees from the Harbin Institute of Technology, Harbin, China, in 1992 and 1995, respectively, and the Ph.D. degree in electrical and computer engineering from the Memorial University of Newfoundland, St. John's, NL, Canada, in 2004. He is currently a Full Professor with the Department of Electrical and Computer Engineering, Faculty of Engineering and Applied Science, Memorial University of Newfoundland. His research interests include ad hoc and wireless sensor networks, wireless communications and networking, underwater communications and networks, switching and routing, and broadband communication networks. He is a Senior Member of the IEEE and its Communications, Computer, Ocean Engineering, and Vehicular Technology Societies. He was a recipient of the Best Paper Award at the International Conference on Ad Hoc Networks (ADHOCNETS) 2018, the IEEE GLOBECOM 2017, and the IEEE International Conference on Communications (ICC) 2010. He was the General Co-Chair of the 2019 International Conference on Artificial Intelligence for Communications and Networks and the International Conference on Wireless Networks and Mobile Communications in 2017 and 2019. He was the Technical Program Committee Co-Chair of the 2020 International Conference on Computing, Networking, and Communications, ADHOCNETS 2019, the 2017 Wireless Internet Conference, the Annual International Conference on Modeling, Analysis, and Simulation of Wireless and Mobile Systems in 2013 and 2014, the International Conference on Wireless and Mobile Computing, Networking, and Communications in 2011, and the Biennial Symposium on Communications in 2010. He was also the Co-Chair of

various technical symposia or tracks of many international conferences, including the IEEE ICC and GLOBECOM, the International Conference on Communications, the Wireless Communications and Networking Conference, the Vehicular Technology Conference, and the International Wireless Communications and Mobile Computing Conference. He is an Editorial Board Member of the *Wiley Wireless Communications and Mobile Computing*, the *Journal of Networks*, and the *KSII Transactions on Internet and Information Systems*, as well as an Associate Editor of the *Wiley Security and Communication Networks*. He is a Registered Professional Engineer in Canada.



Fan Jiang received the B.E. degree in communication engineering from the University of Electronic Science and Technology of China, Chengdu, China, the M.E. degree in communication and information systems from Southeast University, Nanjing, China, and the Ph.D. degree from the Memorial University of Newfoundland (MUN), St. John's, NL, Canada, in 2010, 2013, and 2018, respectively. Since June 2019, he has been with the Laboratory for Information and Decision Systems (LIDS), Massachusetts Institute of Technology (MIT), as a Post-Doctoral Fellow. Before that, he was a Teaching/Research Assistant, then a Sessional Instructor, and a Post-Doctoral Fellow at the Faculty of Engineering and Applied Science, MUN. His research interests include signal processing for wireless communications, massive multiple-input multiple-output (MIMO) and millimeter wave systems, as well as localization, tracking, and navigation framework. He has served in a number of international conferences with various roles such as the program co-chair, technical program committee (TPC) member, session chair, and also a reviewer. He is also an active Reviewer for numerous international journals, such as the *IEEE JOURNAL OF SELECTIVE TOPICS IN SIGNAL PROCESSING*, the *IEEE TRANSACTIONS ON WIRELESS COMMUNICATIONS*, the *IEEE TRANSACTIONS ON COMMUNICATIONS*, and the *IEEE TRANSACTIONS ON VEHICULAR TECHNOLOGY*. He has received the Post-Doctoral Fellowship from the Natural Science and Engineering Research Council (NSERC) of Canada in 2019, the Governor General's Gold Medal at MUN in 2018, and the Best Paper Award at the 2017 IEEE Global Communications Conference (Globecom'17).



Jun Zheng received the Ph.D. degree in electrical and electronic engineering from The University of Hong Kong, Hong Kong, in 2000.

He is currently a Full Professor with the School of Information Science and Engineering, Southeast University (SEU), China. Before joining SEU in 2008, he was with the School of Information Technology and Engineering, University of Ottawa, Canada. He has coauthored (First Author) two books published by the Wiley-IEEE Press, and has coauthored nearly 200 technical articles in refereed journals and peer-reviewed conference proceedings. His current research interests include vehicular ad hoc networks, mobile communication networks, wireless sensor networks, focused on network architectures and protocols. He is a Senior Member of the IEEE Communications Society and the IEEE Vehicular Technology Society. He is a co-recipient of an ICC 2014 Best Paper Award, the WCSP 2018 Best Paper Award, and the WiCON 2017 Best Student Paper Award. He serves as a Technical Editor for the *IEEE Communications Magazine* and was the Editor-in-Chief of the *EAI Endorsed Transactions on Mobile Communications and Applications*. He is also an editorial board member of several refereed journals. He has co-edited 12 special issues for different refereed journals and magazines, including the *IEEE Communications Magazine*, the *IEEE NETWORK*, and the *IEEE JOURNAL ON SELECTED AREAS IN COMMUNICATIONS*, all as a Lead Guest Editor. He has served as the founding General Chair of AdHocNets'09, the General Chair of AccessNets'07, and AdHocNets'18-19, and the TPC or Symposium Co-Chair for a number of international conferences and symposia, including the IEEE ICC (2009, 2011, 2015) and GLOBECOM (2008, 2010, 2012, 2018, 2019). He has also served as a Technical Program Committee Member for a number of international conferences and symposiums. He also serves as the Chair of the IEEE Vehicular Technology Society Nanjing Chapter, and the Chair of the IEEE ComSoc Communications Switching and Routing Technical Committee.